Microglial Homeostasis Requires Balanced CSF-1/CSF-2 Receptor Signaling

Violeta Chitu[1], **Fabrizio Biundo**[1], **Gabriel G.L. Shlager**[1], **Eun S. Park**[1,11], **Ping Wang**[2], **Maria E. Gulinello**[3], **Sxölen Gokhan**[4], **Harmony C. Ketchum**[1], **Kusumika Saha**[1,12], **Michael A. DeTure**[5], **Dennis W. Dickson**[5], **Zbignew K. Wszolek**[6], **Deyou Zheng**[7], **Andrew L. Croxford**[8], **Burkhard Becher**[9], **Daqian Sun**[10], **Mark F. Mehler**[4], **E. Richard Stanley**[1,13,*]

[1]Department of Developmental and Molecular Biology, Albert Einstein College of Medicine, Bronx, NY 10461, USA [2]Department of Genetics, Albert Einstein College of Medicine, Bronx, NY 10461, USA [3]Behavioral Core Facility, Dominick P. Purpura Department of Neuroscience, Albert Einstein College of Medicine, Bronx, NY 10461, USA [4]Institute for Brain Disorders and Neural Regeneration, Departments of Neurology, Neuroscience, and Psychiatry and Behavioral Sciences, Albert Einstein College of Medicine, Bronx, NY 10461, USA [5]Department of Neuroscience, Mayo Clinic, Jacksonville, FL 32224, USA [6]Department of Neurology, Mayo Clinic, Jacksonville, FL 32224, USA [7]The Saul R. Korey Department of Neurology, Dominick P. Purpura Department of Neuroscience, and Department of Genetics, Albert Einstein College of Medicine, Bronx, NY 10461, USA [8]Idorsia Pharmaceuticals Ltd., Allschwil 4123, Switzerland [9]Institute of Experimental Immunology, University of Zurich, Zurich 8057, Switzerland [10]Department of Cell Biology, Albert Einstein College of Medicine, Bronx, NY 10461, USA [11]Present address: MSB 7.147, Department of Neurosurgery, University of Texas Health Science Center at Houston, 6431 Fannin Street, Houston, TX 77030, USA [12]Present address: Institut Cochin, INSERM U1016, CNRS UMR8104, Université Paris Descartes, Sorbonne Paris Cité, 27 rue du Faubourg St-Jacques, 75014 Paris, France [13]Lead Contact

SUMMARY

CSF-1R haploinsufficiency causes adult-onset leukoencephalopathy with axonal spheroids and pigmented glia (ALSP). Previous studies in the *Csf1r*^{+/−} mouse model of ALSP hypothesized a central role of elevated cerebral *Csf2* expression. Here, we show that monoallelic deletion of *Csf2*

[*]Correspondence: richard.stanley@einsteinmed.org.

rescues most behavioral deficits and histopathological changes in *Csf1r*^{+/−} mice by preventing microgliosis and eliminating most microglial transcriptomic alterations, including those indicative of oxidative stress and demyelination. We also show elevation of *Csf2* transcripts and of several CSF-2 downstream targets in the brains of ALSP patients, demonstrating that the mechanisms identified in the mouse model are functional in humans. Our data provide insights into the mechanisms underlying ALSP. Because increased *CSF2* levels and decreased microglial *Csf1r* expression have also been reported in Alzheimer's disease and multiple sclerosis, we suggest that the unbalanced CSF-1R/CSF-2 signaling we describe in the present study may contribute to the pathogenesis of other neurodegenerative conditions.

In Brief

ALSP is a dementia caused by dominantly inherited inactivating mutations in the *CSF1R*. Chitu et al. report that *CSF2* expression is increased in ALSP patients. Targeting *Csf2* in ALSP mice prevents behavioral deficits and callosal atrophy and reduces demyelination by normalizing microglial function, identifying CSF-2 as a potential therapeutic target in ALSP.

Graphical Abstract
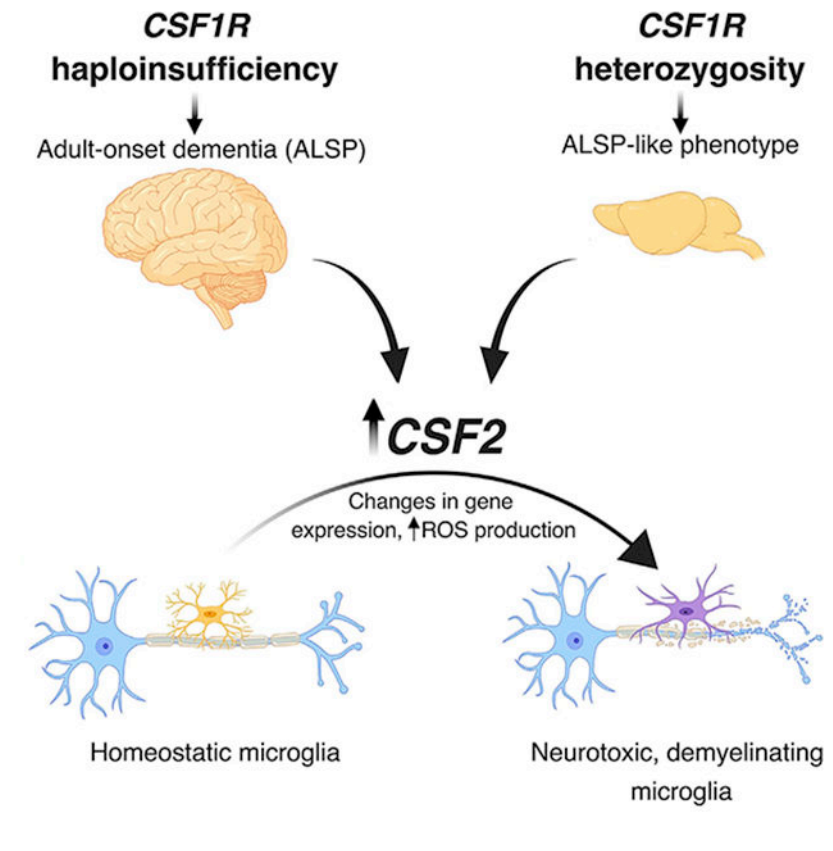
INTRODUCTION

The colony-stimulating factor-1 receptor (CSF-1R) is regulated by two cognate ligands, CSF-1 and interleukin-34; is expressed on microglia; and is required for their development

and maintenance (reviewed in Chitu et al., 2016). Recent studies show that microglia play important roles in the regulation of neuronal development, learning-dependent synaptic pruning, and oligodendrogenesis (Chitu et al., 2016; Hagemeyer et al., 2017). Thus, the microglial CSF-1R may non-cell-autonomously regulate neural lineage cells.

Adult-onset leukoencephalopathy with axonal spheroids and pigmented glia (ALSP), also known as hereditary diffuse leukoencephalopathy with axonal spheroids and pigmented glia or pigmented orthochromatic leukodystrophy, is an autosomal-dominant, neurodegenerative disorder caused by mutations of the *CSF1R* gene (reviewed in Konno et al., 2018). ALSP is characterized by dementia with neuropsychiatric and motor deficits and has an average disease duration of 6.8 years. The discovery of an ALSP patient with a *CSF1R* frameshift mutation that abolished CSF-1R protein expression proved that *CSF1R* haploinsufficiency is sufficient to cause ALSP (Konno et al., 2014).

Similar to ALSP patients, $Csf1r^{+/-}$ mice exhibit behavioral, radiological, histopathological, and ultrastructural alterations associated with microgliosis and demyelination (Chitu et al., 2015). Microgliosis occurred in the absence of a compensatory increase in the expression of CSF-1R ligands. However, in both presymptomatic and diseased mice, microgliosis was associated with an increase in expression of mRNA of the proinflammatory microglial mitogen colony-stimulating factor-2 (CSF-2), also known as granulocyte macrophage CSF (GM-CSF) (Chitu et al., 2015). In the present study, we show that CSF2 expression is also increased in the brains of ALSP patients, and we examine the effect of removal of a single *Csf2* allele on development of ALSP in $Csf1r^{+/-}$ mice.

RESULTS

Monoallelic Targeting of *Csf2* Prevents White Matter Microgliosis in Young $Csf1r^{+/-}$ Mice

Because CSF-2 is a microglial mitogen (Lee et al., 1994), and $Csf1r^{+/-}$ mice exhibit early-onset microgliosis (Chitu et al., 2015), we initially examined the effect of genetic targeting of *Csf2* on Iba-1$^+$ microglia density in young $Csf1r^{+/-}$ mice. Mono-allelic targeting was sufficient to normalize Csf2 mRNA expression and to lower the microglial density in $Csf1r^{+/-}$ mice to wild-type levels (Figures 1A–1C). *Csf2* homozygous deletion showed no additional effects over *Csf2* heterozygosity. Consistent with the low abundance of *Csf2* transcripts in wild-type brains (Figure 1C), Iba-1$^+$ cell densities in $Csf2^{+/-}$ and $Csf2^{-/-}$ mice were not different from those of wild-type mice (Figures 1A and 1B).

To investigate whether CSF-2 drives microgliosis in ALSP mice directly by stimulating its receptor in microglia, we used the $Cx3Cr1^{Cre/+}$ gene targeting system (Yona et al., 2013; Goldmann et al., 2013) to delete a *Csf2rb* allele (Croxford et al., 2015) in myeloid cells and microglia. The mice were examined at 3 months of age, when there is no evidence of demyelination or other pathological changes (Figure S1) that could confound interpretation of the results. Similar to *Csf2* heterozygosity, conditional deletion of a single *Csf2rb* allele was sufficient to prevent white matter microgliosis in young $Csf1r^{+/-}$ mice without altering microglial densities in the wild-type background (Figures 1D and 1E). These data indicate that CSF-2 causes microgliosis in the ALSP model via direct stimulation of microglia.

Increased Expression of *CSF2* in the Brains of ALSP Patients

To investigate whether *CSF2* was elevated in the human disease, we examined the expression of *CSF2* in the periventricular white matter and adjacent gray matter of 5 ALSP patients and 5 matched controls (Table S1). Consistent with the results obtained in mice, the levels of *CSF2* transcripts were almost undetectable in control patients, whereas *CSF2* expression was increased in the gray matter of ALSP patients (Figure 1F).

Monoallelic *Csf2* Inactivation Prevents Loss of Spatial Memory in ALSP Mice

The normalization of microglial density in young mice prompted us to determine the effect of monoallelic *Csf2* inactivation on the development of behavioral deficits in older $Csf1r^{+/-}$ mice. Regardless of genotype, the body weight of males and females increased with age without significant genotype-associated differences (Figure S2), and there were no significant differences in survival up to 18 months of age. To test the effect of *Csf2* heterozygosity on short-term spatial memory, we used object recognition, object placement, and Y-maze paradigms. In the object recognition test, deficits observed in *Csf1r* haploinsufficient mice at 7 months of age were prevented by *Csf2* heterozygosity (double heterozygous [Dhet]) (Figure 2A). In the Y-maze (Figure 2B) and object placement (Figure 2C) tests, deficits apparent at 13–15 months in *Csf1r* haploinsufficient mice were also prevented by *Csf2* heterozygosity. Interestingly, in the latter two tests, deficits were also present in *Csf2* heterozygous mice. Similar results were obtained at 16.5 months of age in a test of long-term memory (object recognition with a 24-h retention interval; Figure 2D). Again, in these older mice, a deficit became apparent in *Csf2* heterozygous mice. These results demonstrate prevention of short- and long- term spatial memory deficits of $Csf1r^{+/-}$ ALSP mice by *Csf2* heterozygosity. However, they also show that *Csf2* heterozygosity on a wild-type (WT) background results in spatial memory deficits with aging.

Csf2 Heterozygosity Prevents Depression-like Behavior in Male ALSP Mice

Previous studies demonstrated male-specific, depression-like behavior in $Csf1r^{+/-}$ mice (Chitu et al., 2015). This phenotype was reproduced with males in the current cohort and prevented by *Csf2* heterozygosity (Figure 2E).

Monoallelic *Csf2* Inactivation Prevents Olfactory Dysfunction in ALSP Mice

Because $Csf1r^{+/-}$ mice exhibit olfactory deficits (Chitu et al., 2015), we explored the contribution of CSF-2 to this phenotype in an odor discrimination test (Figure 3A). Mice of all genotypes exhibited lower exploration of the repulsive odorant and trigeminal stimulant, lime, compared with the attractive pure odorant, vanilla. However, in response to vanilla, WT mice increased their exploration with time, whereas $Csf1r^{+/-}$ mice failed to do so. This phenotype of $Csf1r^{+/-}$ mice was corrected by *Csf2* heterozygosity. To further explore the olfactory response of $Csf1r^{+/-}$ mice to pure odorants, we subjected the mice to an odor threshold assay (Witt et al., 2009) using 2-phenylethanol (Doty et al., 1978; Figure 3B). Although WT control mice were able to detect 2-phenylethanol at a dilution of 10^{-1}, *Csf1r* $^{+/-}$ mice failed to detect the odorant at any concentration. *Csf2* heterozygosity restored detection to $Csf1r^{+/-}$ mice at a threshold of 10^{-2}. These results indicate that the response of $Csf1r^{+/-}$ mice to pure odorants is impaired and that monoallelic *Csf2* inactivation alleviates

this phenotype. *Csf2* heterozygous mice were unable to detect 2-phenylethanol but responded normally to vanilla. The basis of this selective impairment is unclear.

Inactivation of a Single *Csf2* Allele Partially Improves the Motor Coordination Deficits of Female *Csf1r*$^{+/−}$ Mice

Balance beam studies have shown that older *Csf1r*$^{+/−}$ mice possess motor deficits (Chitu et al., 2015). This phenotype was reproduced with female *Csf1r*$^{+/−}$ mice. In contrast, Dhet mice were indistinguishable from the WT (p = 0.99) (Figure 3C). Similar to their behavior in the balance beam test, female but not male *Csf1r*$^{+/−}$ mice had increased ataxia scores (Guyenet et al., 2010; Figure 3D) that were not attenuated by *Csf2* heterozygosity. Furthermore, *Csf2* heterozygosity alone produced an ataxic phenotype. Overall, these results show that *Csf1r*$^{+/−}$ mice have a female-specific motor deficit and that targeting *Csf2* improves motor coordination on the balance beam but fails to improve ataxic behavior.

Csf2 Heterozygosity Prevents Cerebral but Not Cerebellar Microgliosis of *Csf1r*$^{+/−}$ Mice

Examination of the effects of inactivation of a single *Csf2* allele in 18-month-old symptomatic *Csf1r*$^{+/−}$ mice revealed that *Csf2* heterozygosity prevented the increase in Iba-1$^+$ cells in all gray and white matter tracts examined, with the exception of the cerebellum (Figures 4A and 4B). A remarkable feature was the presence of periventricular patches of high microglial density in the callosal white matter (Figures S3A and S3B). Examination of multiple sagittal sections revealed that microglial patches were more frequently encountered in *Csf1r*$^{+/−}$ mice than in WT mice and that their frequency was normalized in *Csf1r*$^{+/−}$; *Csf2*$^{+/−}$ *Dhet* mice (Figure S3B). Morphometric analysis showed that microglia in the white matter patches of *Csf1r*+/− mice had fewer ramified processes than those of WT mice (Figures 4C and 4D), suggestive of an activated state. The ramified morphology was restored in *Dhet* mice. In contrast, cortical microglia showed no significant difference in ramification compared with the WT (Figures 4C and 4E).

Absence of Leukocytic Infiltration in the Brains of *Csf1r*$^{+/−}$ Mice

Overexpression of *Csf2* in peripheral helper T cells has been reported to promote monocytic infiltration in the brain (Spath et al., 2017), which could contribute to expansion of Iba1+ cells (Greter et al., 2015). To address the contribution of peripheral monocytes, we performed an unbiased flow cytometry analysis of all CD45$^+$ cells in the brains of 15-month-old mice (Figure 4F; Figure S4). This revealed that, in WT and *Csf1r*$^{+/−}$ mice, most Ly6G$^-$ CD45$^+$ cells were CD11b$^+$ CD45^{low} P2ry12^{high}, a profile that identifies brain-resident microglia (Greter et al., 2015; Butovsky et al., 2014). Consistent with this, nearly 100% of Iba1$^+$ cells expressed P2ry12 in all brain regions tested (Figures 4G and 4H). Analysis of the leukocyte populations revealed that *Csf1r*$^{+/−}$ mice did not exhibit increased CD45^{high} CD11b$^+$ P2ry12$^-$ Ly6- C^{low} macrophages/dendritic cells or evidence of increased infiltration of P2ry12$^-$ Ly6G$^+$ granulocytes, CD45^{high} CD11b$^+$ P2ry12$^-$ Ly6C^{hi} monocytes, or various lymphocyte populations compared with WT mice (Figure 4F). The presence of an unusual population of Ly6G$^+$ P2ry12^{high} cells that presumably represent an activated state of microglia (G$^+$μG; Figure 4F; Figure S4) was also detected in aged mice of both genotypes (p = 0.73 versus the WT). Furthermore, in *Cx3Cr1*$^{GFP/+}$; *Ccr2*$^{RFP/+}$ mononuclear phagocyte reporter mice (Mizutani et al., 2012), regardless of genotype or region, the majority of brain

mononuclear phagocytes were green fluorescent protein (GFP) single-positive and identified as resident microglia (Figures 4I and 4J). The proportions of red fluorescent protein (RFP) (*Ccr2*) single-positive monocytes and of cells expressing both monocytic (*Ccr2*) and microglial (P2ry12) markers in *Csf1r*^{+/−} mice were comparable with the WT (Figures 4I and 4J). These data indicate that there is no increase in leukocytic infiltration in *Csf1r*^{+/−} mice. Together with the data shown in Figures 1D and 1E, these results indicate that expansion of Iba1^{+} cells occurs by direct stimulation of resident microglial proliferation by CSF-2.

Gene Expression Changes in *Csf1r*^{+/−} Microglia Suggest a Maladaptive Phenotype

To determine how reductions in *Csf1r* or *Csf2* expression, alone or in combination, affect microglial function in aged (21-month-old) mice, we analyzed the changes in the transcriptome of cerebral Tmem119^{+} microglia compared to WT controls. *Csf1r* heterozygosity led to differential expression of 496 genes, comprising 237 upregulated genes (URGs) and 259 downregulated genes (DRGs) (Table S2; Figure 5A). Functional enrichment analysis revealed that a significant proportion of the *Csf1r*^{+/−} URGs encoded membrane (57), extracellular (39), and mitochondrial (16) proteins (Table S3). In contrast, the innate immunity cluster contained only four URGs (*Tgtp1*, *Ly86*, and the complement proteins *C1qb* and *C1qc*). Among the URGs encoding extracellular proteins were transcripts for the secreted inducer of senescence Augurin (*Ecrg4*) (Kujuro et al., 2010), the neuropeptide Tac2 (Andero et al., 2016), and the CSF-2-induced proinflammatory chemokine Ccl17 (Achuthan et al., 2016; Figure 5B). Other upregulated transcripts included those encoding several mitotoxic (*Apoo*, *Mrps6*, *Nr2f2*, and *Coq7*) (Turkieh et al., 2014; Sultan et al., 2007; Wu et al., 2015; Lapointe and Hekimi, 2008) and neurodegeneration-related (*Syngr1*, *Cst7*, *Trem2*, *Spp1*, and *Ch25h*) (Hegyi, 2017; Ma et al., 2011; Krasemann et al., 2017; Shin et al., 2011) protein products (Figures 5B, 5F, and 5H). Interestingly, *Csf1r* heterozygosity did not reduce the expression of known neurotrophic factors by microglia; rather, it enhanced the expression of genes encoding neurturin, neudesin, midkine, IGF2, and vascular endothelial growth factor B (VEGFB) (Figure 5B; Table S4), suggesting that microglial neurotrophic functions were not impaired.

Analysis of the DRGs showed that approximately 50% (132 of 259) of these encode membrane proteins (Table S3), including proteins with anti-inflammatory activity, such as *Thbd*, *Dpep2*, *Pirb*, *Cd244*, *Il4ra*, and *Il10ra* (Wolter et al., 2016; Habib et al., 2003; Zhang et al., 2005; Georgoudaki et al., 2015; Mori et al., 2016; Lobo-Silva et al., 2016; Figures 5B and 5F). Consistent with downregulation of interleukin-10 (IL-10) receptor signaling in *Csf1r*^{+/−} microglia, its downstream signaling mediator *Stat3* and several IL-10 transcriptional targets (*Ddit4*, *Nfil3*, and *Tsc22d3*) (Ip et al., 2017; Lang et al., 2002; Berrebi et al., 2003; Hoppstädter et al., 2015) were also downregulated (Figures 5B and 5F).

Other potentially relevant downregulated genes encode transcripts associated with Alzheimer's disease (*Sorl1*) (Nicolas et al., 2016), leukodystrophy (*Abcd1* and its downstream mediator of pathology, *Ch25h*) (Gong et al., 2017; Jang et al., 2016), and the CSF-2 target gene *Pkch*, encoding protein kinase Cη, a regulator of lipid metabolism and suppressor of nitrous oxide (NO) production by macrophages (Torisu et al., 2016; Ozawa et al., 2016; Figure 5B).

Pathway analysis revealed that the transcriptomic changes associated with *Csf1r* heterozygosity are consistent with activation of the Rho GDP-dissociation inhibitor (RhoGDI) signaling and liver X receptor/retinoid X receptor (LXR/RXR) pathways (Figure 5E; Table S5). The LXR/RXR pathway has been reported to increase cholesterol efflux and repress Toll-like receptor 4 (TLR4)-induced genes (Hiebl et al., 2018) but also promote inflammasome activation in microglia (Jang et al., 2016). However, inhibition of classical pro-inflammatory pathways, such as the acute phase response and nuclear factor κB (NF-κB) signaling, as well as of TREM1 signaling, which sustains inflammation (Owens et al., 2017), was also predicted (Figure 5E; Table S5), suggesting that $Csf1r^{+/-}$ microglia are not pro-inflammatory. Analysis of the biological processes affected by *Csf1r* heterozygosity predicted active neurodegeneration, increased cellular protrusions and microtubule dynamics, as well as elevated paired-pulse facilitation of synapses (Figure 5F; Table S6).)

To further explore how these transcriptomic changes are relevant to the neuropathology, we intersected our gene list with publicly available datasets showing changes in the microglial transcriptome in other mouse models of neurodegenerative disease, including models of Alzheimer's disease (presenilin/amyloid precursor protein [PS-APP], AD 5xFAD, APPswe/PS1dE9), tauopathy (Tau_P301S), amyotrophic lateral sclerosis (ALS), rapid neurodegeneration (CK-p25), and spinocerebellar ataxia ($Mfp2^{-/-}$) (Friedman et al., 2018; Keren-Shaul et al., 2017; Mathys et al., 2017; Figure 5H). A list showing genes similarly regulated and their functions is provided in Table S7. The comparison shows that 29% of the $Csf1r^{+/-}$ DEGs were similarly regulated in at least one other neurodegenerative disease, with the most extensive overlap occurring with the APPswe/PS1dE9 Alzheimer's disease model, followed by changes related to early neurodegeneration (CK-p25 early cluster 7) and ALS. Consistent with this overlap, *Csf1r* expression was downregulated in microglia isolated from mouse models of Alzheimer's disease and ALS (Figure 5H). Changes occurring under most neurodegenerative conditions were high expression of a group of transcripts encoding the lysososmal cathepsin inhibitor Cystatin F (*Cst7*) (Ma et al., 2011); osteopontin (*Spp1*), an opsonin for cell debris (Shin et al., 2011); and cholesterol 25-hydroxylase *(Ch25h)*, which, through its product 25-hydroxycholesterol, activates the LXR pathway and promotes reactive oxygen species (ROS) production and inflammation (Jang et al., 2016). Underexpression of neuroprotective (*Clec4a1* and *Il16*; Flytzani et al., 2013; Shrestha et al., 2014) and anti-inflammatory (*Klf2*, *Gramd4*, *Ddit4*, *Pirb*, and *Tsc22d3*; Roberts et al., 2017; Ip et al., 2017; Kimura et al., 2015; Zhang et al., 2005; Berrebi et al., 2003) transcripts was observed in ALSP and at least three other conditions (Figure 5H).

Together, our data suggest that *Csf1r* heterozygosity does not produce a neurotrophic defect or overt inflammatory activation of microglia. Rather, the transcriptional profile predicts a maladaptive microglial phenotype (Figure 6A). A summary of the pathways that could contribute to disease pathology is presented in Figure 6B.

Csf2 Heterozygosity Upregulates Antioxidant and Anti-inflammatory Signaling in Microglia

As described above, *Csf2* insufficiency alone also impaired cognition (Figure 2) and partially affected olfaction and motor coordination (Figure 3). However, these phenotypes were not accompanied by microgliosis in $Csf2^{+/-}$ mice. Thus, we examined the effect of

Csf2 heterozygosity on microglia. Compared with WT controls, *Csf2* heterozygosity dysregulated the expression of 1,168 genes (372 URGs and 796 DRGs; Figure 5A; Table S1). Most of the top differentially expressed transcripts encode products still uncharacterized or pseudogene transcripts (Figure S5A). Among the top upregulated transcripts were those encoding the proinflammatory cytokine CCL3 and the matrix metalloproteinase MMP11. The myelin-degrading MMP12 (Hansmann et al., 2012) was also upregulated (Figure S5D). Like *Csf1r*^{+/−} microglia, *Csf2*^{+/−} microglia downregulated the expression of several anti-inflammatory genes (Figures S5A and S5D). Remarkably, *Csf2*^{+/−} microglia reduced the expression of *Il4ra* but not of *Il10ra* (Figure S5D; Tables S2 and S8).

Analysis of pathways uniquely affected by *Csf2* heterozygosity showed activation of the antioxidant vitamin C pathway; of peroxisome proliferator-activated receptor (PPAR) signaling, which regulates lipid metabolism and is anti-inflammatory (Wahli and Michalik, 2012); and of the complement system, which has a well-established role in synapse loss in neurodegenerative disease (Hajishengallis et al., 2017; Stephan et al., 2012). Among the top predictions for inhibited pathways, we found dendritic cell maturation, neuroinflammation, lipopolysaccharide (LPS), and induced nitric oxide synthase (iNOS) signaling (Figure S5B). Analysis of biological processes selectively affected by *Csf2* heterozygosity predicted increased inflammation and encephalitis, which were paradoxically associated with decreased leukocyte infiltration as well as decreased activation of neuroglia and microglia (Figure S5C). These data suggest that the neuropathology in *Csf2*^{+/−} mice is not associated with classically defined inflammatory activation (i.e., increased proinflammatory cytokine and iNOS expression). CSF-2 insufficiency increases activation of the complement system and expression of matrix metalloproteinases (MMPs), both of which could affect neuronal network structure and function. However, it also causes activation of antioxidant (vitamin C antioxidant pathway, upregulation of *Prdx4*) and lipid metabolic (PPAR signaling) pathways that are expected to reduce oxidative stress and inflammation.

Targeting *Csf2* in ALSP Mice Attenuates Microglial Dysfunction and Oxidative Stress

Investigation of the effect of reduction of CSF-2 availability revealed a large decrease in microglial transcriptomic changes of *Csf1r*^{+/−};*Csf2*^{+/−} microglia (254 DEGs, 54 URGs, and 200 DRGs) compared with *Csf1r*^{+/−} microglia (Figure 5A). Indeed, hierarchical clustering of samples based on DEGs grouped *Csf1r*^{+/−} and *Csf2*^{+/−} apart from the Dhet samples, which were more related to WT samples (Figure 5G). Consistent with this, pathway analysis predicted restoration of RhoGDI and LXR/RXR signaling and attenuation of the neurodegenerative phenotype (Figures 5E and 5F). Furthermore, 86% of the transcriptional changes common to ALSP and other neurodegenerative conditions were eliminated in *Csf1r*^{+/−};*Csf2*^{+/−} microglia (Figure 5H), including the expression of gene products that suppress mitochondrial fitness and enhance oxidative stress (e.g., *Ch25h*, *Ddit4*, *Il10ra*, *Apoo*, and *Coq7*). Consistent with this, monoallelic inactivation of *Csf2* in *Csf1*^{+/−} mice reduced poly ADP-ribosylation, a marker of oxidative stress, in periventricular white matter microglial patches (Figures 6C and 6D).

The *Cst7*-encoded protein Cystatin F is a microglial marker of ongoing demyelination with concurrent remyelination (Ma et al., 2011). As predicted by the changes in *Cst7* transcript

abundance, Cystatin F protein was readily detected in the callosal microglial patches present in *Csf1r*^{+/−} brains, but its staining in Dhet brains was not significantly different from WT staining (Figure 5D). Thus, targeting CSF-2 improves microglial homeostatic functions.

Increased Expression of CSF-2 Target Genes Potentially Relevant to Pathology in the White Matter of ALSP Patients

To determine whether similar gene expression changes occur in ALSP patients, we isolated RNA from the callosal white matter of ALSP patients and control (Table S1) brains and performed real-time qPCR. Several transcripts potentially relevant to neurodegeneration, demyelination, and oxidative stress were also upregulated in the white matter of ALSP patients (Figure 6E). These results identify putative common contributors to the pathology of ALSP and of other demyelinating and neurodegenerative diseases.

Monoallelic *Csf2* Inactivation on the ALSP Background Improves Callosal Myelination

Reduction of expression of the demyelination marker Cystatin F by targeting *Csf2* prompted us to examine the ultrastructure of the *corpora callosa* of all genotypes by transmission electron microscopy. Examination of cross-sections showed that *Csf1r*^{+/−} fibers have higher G-ratios than WT fibers, indicative of demyelination followed by remyelination (Figures 7A–7C). Higher G-ratios were also observed in *Csf2*^{+/−} samples (Figures 7A, 7B, and 7E). The G-ratios of callosal fibers in Dhet mice were not significantly different from those of WT fibers (Figures 7A, 7B, and 7D). Consistent with this, staining for myelin basic protein (MBP) was reduced in the *corpus callosum* of *Csf1r*^{+/−} mice and the reduction was prevented by targeting *Csf2* (Figure 7F). Other white matter tracts (fimbria and cerebellar white matter), although trending similarly, were not significantly affected (Figure 7F). Changes in myelination did not result from decreased availability of platelet derived growth factor receptor-α^+ (PDGFRα^+) early oligodendrocyte precursors or of mature CC1$^+$ oligodendrocytes, which were paradoxically increased (Figure 7G). Examination of age-related changes in myelin compaction revealed significantly increased myelin degeneration in *Csf1r*^{+/−} mice that was not rescued by *Csf2* heterozygosity (Figure 7H). In terms of axonal pathology, the data reflect a lack of protective effects of *Csf2* targeting on neurodegeneration (Figure 7I). Consistent with the overall lack of protection against neurodegeneration, *Csf2* heterozygosity did not attenuate the loss of neuronal nuclei$^+$ (NeuN$^+$) mature neurons in cortical layer V (Figures 7J and 7K). Together, these data indicate that *Csf2* heterozygosity rescues myelination but is not sufficient to prevent neurodegeneration and exacerbation of age-related myelin degeneration in ALSP mice.

Csf2 Heterozygosity Normalizes the Callosal Volume in *Csf1r* [+/−] Mice

Because *Csf2* heterozygosity in the ALSP background normalized the G-ratios, we examined whether this resulted in attenuation of white matter loss using MRI. Compared with the WT, callosal volumes were lower in *Csf1r*^{+/−} mice, and *Csf2* heterozygosity prevented callosal atrophy (Figure 7L). In contrast, *Csf2* heterozygosity did not cause a reduction in callosal volume.

DISCUSSION

In a previous study (Chitu et al., 2015), we showed that microglial densities were elevated in several brain regions of young and old *Csf1r*^{+/−} ALSP mice and associated with increased expression of *Csf2*, encoding the microglial mitogen CSF-2. Aside from its mitogenic activity, CSF-2 primes neurotoxic (Fischer et al., 1993) and demyelinating (Smith, 1993) responses in microglia. Because *CSF2* expression is also elevated in post-mortem ALSP brains (Figure 1F), we reasoned that CSF-2 plays an important role in ALSP pathogenesis. Indeed, we show that *Csf2* heterozygosity rescues the olfactory, cognitive, and depression-like phenotypes of *Csf1r*^{+/−} mice and ameliorates the motor coordination deficits (Figures 2 and 3). *Csf2* targeting also reduces microgliosis (Figures 1A, 1B, 4A, and 4B) and a hallmark feature of ALSP, demyelination (Figures 7A–7D and 7F). Although, in the CNS, the CSF-2 receptor is expressed on neural lineage cells (Reed et al., 2005; Baldwin et al., 1993) and microglia, several lines of evidence suggest that *Csf2* deletion ameliorates neuropathology by acting on microglia rather than on neural lineage cells. First, the reported neuroprotective (Schäbitz et al., 2008) and oligodendrogenic (Baldwin et al., 1993) activities of CSF-2 suggest that its targeting in ALSP should be detrimental rather than protective. However, we found that *Csf2* heterozygosity did not exacerbate loss of layer V neurons, indicating that its neuroprotective actions are negligible in the context of ALSP. Furthermore, in the ALSP mouse, demyelination is paradoxically associated with an expansion of oligodendrocyte precursors and APC[+] oligodendrocytes (Figure 7G). Targeting of *Csf2* prevents the increase in oligodendrocytes and oligodendrocyte precursors in ALSP mice (Figure 7G), but this finding cannot explain how it attenuates the loss of myelin. One conceivable explanation is that *Csf2* heterozygosity prevents microgliosis (Lee et al., 1994) and priming of demyelinating (Smith, 1993) and neurotoxic (Fischer et al., 1993) responses in microglia. A direct investigation of the contribution of CSF-2 signaling in different cell types to pathology requires conditional targeting of its receptor, *Csf2ra*, which is presently not possible because of the absence of a specific genetic model. An acceptable approximation is conditional targeting of *Csf2rb*, which encodes the common subunit of CSF-2, IL-3, and IL-5 receptors (Croxford et al., 2015), using lineage-specific *Cre* drivers. Using this approach, we showed that attenuation of CSF-2 signaling in CX3CR1-expressing cells (i.e., mononuclear phagocytes and microglia) was sufficient to prevent white matter microgliosis in young mice (Figures 1D and 1E). Based on this observation and on the finding that monocyte-derived cells do not significantly contribute to the widespread microgliosis in aged *Csf1r*^{+/−} mice (Figures 4F–4J), we conclude that CSF-2 triggers microgliosis via direct signaling in CNS-resident microglia. Thus, although a contribution of CSF-2 signaling in other cell types cannot be formally excluded, current data suggest that the CSF-2-mediated dysregulation of microglial function plays a central role in the pathology of ALSP mice. Consistent with this, transcriptomic analysis revealed that *Csf2* heterozygosity suppressed a high proportion of the transcriptomic changes occurring in *Csf1r*^{+/−} microglia, including the expression markers of oxidative stress and demyelination (Figures 5 and 6 and a more detailed discussion below).

Transcriptomics analysis suggests that clearance of apoptotic cells and myelin debris triggers maladaptive responses in *Csf1r*^{+/−} microglia. Relevant changes include

overexpression of TREM2, an innate immune receptor expressed on microglia that promotes clearance of apoptotic neurons and myelin debris (Poliani et al., 2015). Recent work indicates that, following uptake of apoptotic neurons or neuronal debris, TREM2 increases the expression of oxidative stress markers and complement components and suppresses the homeostatic function of microglia (Linnartz-Gerlach et al., 2019; Krasemann et al., 2017). The molecular mechanism could involve suppression of mitophagy either directly (Ulland et al., 2017; Wang et al., 2019) or as an indirect consequence of overloading of the degradative pathway by the ingested myelin (Safaiyan et al., 2016). Furthermore, as observed in the mouse model (Figure 5C), overexpression of *TREM2* also occurs in the white matter of ALSP patients (Figure 6E), where others have documented the presence of lipid-laden macrophages (Tada et al., 2016; Lin et al., 2010). Thus, decreased autophagy may contribute to ALSP pathology, and the benefits of stimulation of autophagy should be further explored.

Dysregulation of lipid metabolism may also contribute to ALSP. One of the genes downregulated in $Csf1r^{+/-}$ microglia encodes the very-long-chain fatty acid transporter ABCD1. Mutations in *ABCD1* cause X-linked adrenoleukodystrophy, a demyelinating disease associated with microglial dysfunction mediated by overexpression of *Ch25h* encoding cholesterol 25 hydroxylase (Gong et al., 2017; Jang et al., 2016). The product of cholesterol 25 hydroxylase (CH25H), 25-hydroxycholesterol (25-HC), is an activating ligand of LXR, providing an explanation for activation of the LXR/RXR pathway in $Csf1r^{+/-}$ microglia (Figure 5E). *In vivo*, 25-HC has been reported to promote oligodendrocyte death, and *in vitro*, 25-HC stimulates IL-1β secretion by microglia in a mitochondrial ROS- and LXR/RXR-dependent manner (Jang et al., 2016). Expression of *CH25H* was also elevated in the white matter of ALSP patients (Figure 6E), suggesting that dysregulation of cholesterol metabolism in microglia may contribute to the pathology of ALSP.

Double *Csf1r* and *Csf2* heterozygosity eliminates the changes in most canonical pathways and biological processes produced by either *Csf1r* or *Csf2* heterozygosity alone (Figures 5E and 5F; Figures S5B and S5C), including activation of the LXR/RXR pathway (Figure 5E). In the context of ALSP, *Csf2* heterozygosity virtually restores microglial function, resulting in attenuation of oxidative stress, improvement of callosal myelin thickness, and restoration of callosal volume (Figures 5, 6, and 7). Together with normalization of most behavioral phenotypes of $Csf1r^{+/-}$ mice by monoallelic targeting of *Csf2*, these studies clearly identify CSF-2 as a therapeutic target in ALSP. In addition, this work demonstrates that reduction of either CSF-1R or CSF-2 signaling impairs microglia function and homeostasis of the aging CNS and that rebalancing the signals is beneficial. Increased *CSF2* levels and decreased microglial *Csf1r* expression have been reported in Alzheimer's disease (Figure 5; Tarkowski et al., 2001) and multiple sclerosis (Kostic et al., 2018; Werner et al., 2002). Thus, apart from ALSP, the unbalanced CSF-1R/CSF-2 signaling described here may contribute to the pathogenesis of other neurodegenerative conditions.

STAR★METHODS

LEAD CONTACT AND MATERIALS AVAILABILITY

Further information and requests for resources and reagents should be directed to and will be fulfilled by Dr. E. Richard Stanley (richard.stanley@einsteinmed.org). The study did not generate new unique reagents.

EXPERMIENTAL MODEL AND SUBJECT DETAILS

In vivo animal studies

Mouse Strains, Breeding and Maintenance: All *in vivo* experiments were conducted in accordance with the National Institutes of Health regulations on the care and use of experimental animals and approved by the Albert Einstein College of Medicine Institutional Animal Care and Use Committee. The generation, maintenance and genotyping of $Csf1^{+/-}$ mice was described previously (Dai et al., 2002). $Csf2^{+/-}$ mice (Dranoff et al., 1994) were a gift from Dr. Glenn Dranoff and were genotyped using a PCR procedure developed by the Dranoff laboratory that utilizes the primers listed in the Key Resources table. Both lines were backcrossed for more than 10 generations onto the C57BL6/J background. Cohorts were developed from the progeny of matings of $Csf1r^{+/-}$ to $Csf2^{+/-}$ mice, randomized with respect to the litter of origin. At 3 months of age, they were transferred from a breeder diet (PicoLab Rodent Diet 20 5058) to a lower fat maintenance diet (PicoLab Rodent Diet 20 5053). This prevented the increase in body weight in $Csf1r+/-$ mice compared with wild-type mice observed in our earlier study (Chitu et al., 2015) and was also associated with delayed onset of spatial memory deficits (from 7 to 14 months of age) and absence of motor impairment in male $Csf1r^{+/-}$ mice. $Csf2rb^{fl/fl}$ mice (Croxford et al., 2015) were provided by Dr. Burkhard Becher, via Dr. William R Drobyski, Medical College of Wisconsin, $Cx3Cr1^{GFP/+}; Ccr2^{RFP/+}$ mononuclear phagocyte reporter mice (Saederup et al., 2010) were a gift from Dr. Susanna Rosi, Kavli Institute for Fundamental Neuroscience, University of California, San Francisco and $Cx3Cr1^{Cre/+}$ mice (Yona et al., 2013) were a gift from Dr. Marco Prinz, Institute of Neuropathology, Freiburg University Medical Centre, Freiburg, Germany. The age and sex of animals used in each experiment is indicated in Table S9.

Human studies—Frozen brain tissue blocks containing periventricular white matter were obtained from the Mayo Clinic Brain Bank. Consent for autopsy was obtained from the legal next-of-kin. Studies involving autopsy tissue are exempt from human subjects research (Health and Human Services Regulation 45 CFR Part 46). Information on the ALSP patients harboring *CSF1R* mutations and control cases included in this study is summarized in Table S1. Upon removal from the skull according to standard autopsy pathology practices, the brain was divided in the mid-sagittal plane. Half was fixed in 10% neutral buffered formalin, and half was frozen in a −80°C freezer, face down to avoid distortion. The frozen brain was shipped on dry ice to the Neuropathology Laboratory at Mayo Clinic where it was stored in −80°C freezer. Frozen tissue was partially thawed before dissection and slabbed in a coronal plane at about 1-cm thickness. Regions of interest were dissected from the frozen slabs and placed in microcentrifuge tubes before being shipped to the research laboratory on dry ice. At all steps, the fresh and frozen tissue was handled with Universal Precautions.

METHOD DETAILS

Cognitive Assessment—Behavioral studies were carried out by blinded operators. Recognition memory was assessed as time exploring a familiar and a novel object, using the novel object recognition test (Ennaceur and Delacour, 1988). The experimental groups were first tested at 7 months of age for short-term memory (1h-retention interval), then at the age of 16 months for long-term memory (24h-retention interval). Mice explored two identical objects (familiarization) for 4 min (1h-retention) or for 10 min (24h-retention) during the training stage. Mice were then exposed to one of the familiar objects and to a novel object for 3 min (1h-retention) or 5 min (24h-retention) during the testing stage. Each mouse was placed in the center of a 40 cm x 40 cm open field box and allowed to explore the objects freely during each stage. Two different pairs of non-toxic objects were used for each experiment. The novelty of the objects (i.e., novel versus familiar) was counter-balanced within each genotype and the objects were previously validated for equivalent exploratory valence.

Spatial recognition memory was measured at 13.5 months of age in the two-trial test version of the Y-maze (Biundo et al., 2016). Briefly, during the training trial, one of the arms of the maze was closed, and mice were placed into one of the two remaining arms of the maze (start arm) and allowed to explore the open two arms for 10 min. After a 1h inter-trial interval, the blocked arm was opened (novel arm), and mice were placed in the start arm and allowed to explore freely all three arms of the maze for 5 min (test trial).

Spatial recognition memory was also tested at 14.5 months of age in the object placement test (Ennaceur and Delacour, 1988). Each mouse was exposed for 7 min to two identical objects placed in a 40 cm x 40 cm open field box. Four different visual cues were hung on the walls of the box to permit each mouse to orient within the arena. During the training stage, the objects were placed at a distance of 10 cm from one another. After an interval of 25 minutes, one of the objects was displaced into a novel position (15 cm distance, 90 degree angle) and each mouse was returned to the same box to explore the objects for 5 min (testing).

Olfactory Assessment—Olfactory discrimination was tested at 8 months of age. Each mouse was exposed to two non-social odors, a pure odorant attractant (vanilla extract) and an aversive odorant (lime extract), and to water as control. Each odorant was adsorbed in a filter paper placed in a 30-mm Petri dish (5 ul of lime extract, 30 ul of vanilla extract, or 30 ul of water per filter). During the test, a single mouse was placed in the center of a 40 cm x 40 cm box in which the dishes containing odorant filters were placed in two opposite corners of the box, while two dishes containing water-adsorbed-filters were placed in the remaining opposite corners. All the dishes were covered until each mouse was placed in the box. Mice were allowed to explore for 10 minutes. Time exploring each odorant and water was recorded during two 5-minute consecutive bins.

The ability of mice to explore a pure odorant was further assessed in 10-month-old mice using the olfactory threshold test in which exploration of the pure odorant, 2-phenylethanol, or mineral oil carrier, applied to a cotton tip, is assessed (Doty et al., 1978; Witt et al., 2009). All experiments were carried in a plexiglas box placed in a odor-free ventilated hood. Before

testing, each mouse was habituated to the cotton tip by being exposed five times to mineral oil. During the testing trials, the experimental groups were exposed to 5 ten-fold serial dilutions (from 10^{-4} to $10°$) of the odorant. Between each dilution of odorant mice were exposed to mineral oil. In each condition, the cumulative time spent exploring the odorant or mineral oil over a 1 minute period was recorded.

Depression-like Behavior—Depression-like behavior was assessed as immobility, using the Porsolt Forced Swim Test (Porsolt et al., 1977a; Porsolt et al., 1977b). Briefly, each mouse was placed into a 4-l beaker filled with warm water (24°C) for 10 minutes and the duration of immobility during three, 3-minute, consecutive bins was recorded.

Motor Coordination and Ataxic Behavior—Motor coordination was assessed as the number of slips made while crossing a round, wooden balance beam (Gulinello et al., 2008). Briefly, each mouse was allowed to walk along a 1.6 cm diameter, 1 m long beam placed between two holders 1 m off the ground. Palatable food was placed at the end of the beam as an incentive to cross. The ataxia phenotype was evaluated as the sum of scores in the ledge, the hindlimb clasping and the gait tests, as previously described (Guyenet et al., 2010).

Gene Expression Studies in ALSP Patients—RNA was isolated from either the periventricular white matter or the adjacent gray matter of 5 ALSP patients and 5 control patients (see Table S1) using Trizol and cDNA was prepared using a Super Script III First Strand Synthesis kit (Invitrogen, Carlsbad, CA). Real time PCR was performed using SYBR Green in an Eppendorf Realplex II thermocycler. The primers used are listed in Table S10. Average values from two different blocks of tissue per patient, were used to construct the figures.

Analysis of Microglia and Leukocytes—Microglia and brain leukocytes were analyzed using and adaptation of the protocol described by Legroux et al. (2015). Briefly, mice were perfused with ice-cold PBS containing 10 U/ml heparin. Brains were dissected, minced and digested in 5 mL digestion buffer (2mg/ml Collagenase D, 14 μg/ml DNase I in Hanks' Balanced Salt solution (HBSS)) for 20'at 37°C. Myelin was removed by centrifugation in 37% Percoll in HBSS for 10 minutes at $500 \times g$, without brakes. The cell pellet was washed twice with FACS buffer (2% FCS in PBS), and the Fc receptors were blocked by incubation in FACS buffer containing rat anti-mouse CD16/CD32 (Fc block) for 15 minutes on ice. The cells were stained using the antibodies diluted 1:200 in FACS buffer and incubated overnight at 4°C in the dark. Cells were subsequently washed twice with FACS buffer, resuspended in 1ml FACS buffer containing 2.5 μg/ml DNase I and analyzed in a MoFlo Astrios EQ (Beckman Coulter, IN). The antibodies used for staining are listed in the Key Resources Table and the gating strategy utilized to identify each cell type is shown in Figure S3. Data were analyzed using FlowJo version 10.6.1.

Microglia Isolation and RNA-Seq Analysis—Microglia were isolated by FACS (Bennett et al., 2016). The RNA was extracted using a QIAGEN RNeasy Plus Micro kit and stored at −80°C prior to analysis. We obtained 150 bp paired-end RNA-Seq reads from an Illumina NextSeq 500 instrument. For 3 biological replicates of wild-type, $Csf1r^{+/-}$, $Csf2^{+/-}$, and 2 biological replicates for $Csf1r^{+/-};Csf2^{+/-}$ samples, an average of ~46 million pairs of

reads per sample was obtained. The computational pipeline for identifying differentially expressed genes (DEGs) has been described previously (Wang et al., 2017). Briefly, adapters and low quality bases in reads were trimmed by trim_galore: (http://www.bioinformatics.babraham.ac.uk/projects/trim_galore/). The Kallisto (v0.43.1) software (Bray et al., 2016) was employed to determine the read count and transcripts per kilobase million (TPM) for each gene that was annotated in the GENCODE database (vM15) (Mudge and Harrow, 2015). Then we summed the read counts and TPM of all alternative spliced transcripts of a gene to obtain gene expression levels. To identify DEGs, 14,739 expressed genes with an average TPM > 1 were selected in any of the wild-type, $Csf1r^{+/-}$, $Csf2^{+/-}$ and $Csf1r^{+/-}$;$Csf2^{+/-}$ samples, using the software DESeq2 (Love et al., 2014) and false discovery rate (FDR) < 0.05. For selected genes changes in expression were validated by qPCR, utilizing the primers listed in Table S10. Ingenuity pathway analysis (IPA) (https://digitalinsights.qiagen.com/) was used for canonical pathway analysis.

Comparison of DEGs With Other Datasets—The DEG lists from $Csf1r^{+/-}$ or $Csf2^{+/-}$ samples were compared to the DEG lists generated from other studies of microglia transcriptome changes associated with neurodegeneration (Mathys et al., 2017; Keren-Shaul et al., 2017). In Keren-Shaul et al. (2017) and Friedman et al. (2018), DEGs were defined as FDR < 0.05, as described in the original papers, while in Mathys et al. (2017) DEGs were defined by |z| > 2. The log2(fold-change) of those DEGs were used to generate heatmaps.

MRI Imaging—Mice were imaged on an Agilent Direct Drive 9.4 T MRI system (Agilent Technologies, Santa Clara, CA) as previously described (Chitu et al., 2015). Mice were anesthetized with 1.5% isoflurane in room air, and respiratory rate and oxygenation saturation were monitored and maintained within normal ranges, while body temperature was maintained at 39°C, using a warm air circulator (SA instruments, Bayshore, NY). A 1.8mm actively decoupled surface coil (Doty Scientific, Columbia, SC) was used for acquisition, and a 60 mm ID birdcage volume coil (M2M Imaging, Cleveland, OH) was used for radio frequency transmission. Callosal volumes were measured using MIPAV 7.1.1 freeware (https://mipav.cit.nih.gov/).

Ultrastructural Studies—Callosal sections were obtained as described (Chitu et al., 2015). Briefly, mice were perfused with 30 mL of cold phosphate buffered saline (PBS) containing 10 U heparin/ml followed by 30 mL of 2% paraformaldehyde (PFA) in PBS. The dissected brains were cut into 2 mm thick slices and placed in cacodylate fixation buffer (2% PFA, 2.5% glutaraldehyde in 0.1 M cacodylate buffer, pH 7.4) for 40 min at room temperature. Corpus callosum was dissected, incubated overnight at 4°C in cacodylate fixation buffer, embedded, sectioned, stained and examined by transmission electron microscopy using a FEI Technai 20 transmission electron microscope. The ratio between the diameter of an axon and the mean diameter of the myelinated fiber (G-ratio) was determined on 200 randomly chosen fibers (3–6 animals/ genotype) using ImageJ software (imagej.net). Age-related ultrastructural changes were identified according to the description provided by Peters and Sethares (Alan Peters and Claire Folger Sethares, The fine structure of the aging brain (http://www.bu.edu/agingbrain)) and quantified in 15 different microscopic fields / mouse (3–6 animals/genotype; average neurons/genotype 1118; range 929–1498).

Immunofluorescence Staining of Brain Sections—Brain sections (30 μm thick) were obtained as described (Chitu et al., 2015) and stained using antibodies to ionized calcium binding adaptor molecule 1 (Iba1) (rabbit IgG; Wako Chemicals, Richmond, VA or goat IgG; AbCam, Cambridge, MA), cystatin F (rabbit IgG; Fisher, Pittsburgh, PA), poly(ADP-ribose) (mouse monoclonal, Millipore, Billerica, MA), myelin basic protein (mouse monoclonal, BioLegend, Dedham, MA), PDGFRa (goat polyclonal, Minneapolis, MN), CC1 (a mouse antibody to APC reacting with Quaking 7, Millipore, Danvers, MA) and NeuN (mouse monoclonal, Millipore, Danvers, MA). Rat anti-P2ry12 was a gift from Dr. Oleg Butovsky (Harvard Medical School). Secondary antibodies, conjugated to either Alexa 488, Alexa 594 or Alexa 647, were from Life Technologies (Grand Island, NY). Images were captured using an Nikon Eclipse TE300 fluorescence microscope with NISElements D4.10.01 software. Quantification of cell numbers was performed manually. Quantification of fluorescent areas was performed using ImageJ. Images were cropped and adjusted for brightness, contrast and color balance using Adobe Photoshop CS4.

Microglia morphometry—Brain sections (30 μm thick) were obtained and stained with Iba1 as described in the previous section. Z series stacks were acquired using a Leica SP5 Confocal microscope at 40x magnification with a 2 μm interval between images. Morphometric analysis of microglia was carried out in FIJI on maxiumum intensity projections of tissue sections from 3 mice/genotype using the protocol described by Young and Morrison (2018).

QUANTIFICATION AND STATISTICAL ANALYSIS

Statistical Analyses—Statistical analysis was performed using the GraphPad Prism 7 software (GraphPad, La Jolla, CA, USA). Data were screened for the presence of outliers using the ROUT method, assessed for Gaussian distribution by D'Agostino-Pearson omnibus normality test and analyzed using Student's t test, one-way ANOVA, the Kruskal-Wallis test or two-way ANOVA, as appropriate. Pairwise differences were identified using post hoc multiple comparison tests. The level of significance was set at $p < 0.05$. Data within each group are presented as averages ± standard error of the mean (SEM). Only those differences that have reached statistical significance are indicated on the figures. Sample sizes for each experiment are indicated in the figure legends and more information can be found in Table S9.

DATA AND CODE AVAILABILITY

Data Availability—All data are available in the main text or the supplemental materials. The source data for Figure 4F are available in the Mendeley Database: https:// data.mendeley.com/datasets/7m928vkpht/draft?a=19e92205–6537-4f8b-9278- f2399d5a55ba. RNA Seq data are available in the Gene Expression Omnibus (GEO) database: GSE143823.

Supplementary Material

Refer to Web version on PubMed Central for supplementary material.

ACKNOWLEDGMENTS

REFERENCES

Achuthan A, Cook AD, Lee MC, Saleh R, Khiew HW, Chang MW, Louis C, Fleetwood AJ, Lacey DC, Christensen AD, et al. (2016). Granulocyte macrophage colony-stimulating factor induces CCL17 production via IRF4 to mediate inflammation. J. Clin. Invest 126, 3453–3466. [PubMed: 27525438]

Andero R, Daniel S, Guo JD, Bruner RC, Seth S, Marvar PJ, Rainnie D, and Ressler KJ (2016). Amygdala-Dependent Molecular Mechanisms of the Tac2 Pathway in Fear Learning. Neuropsychopharmacology 41, 2714–2722. [PubMed: 27238620]

Baldwin GC, Benveniste EN, Chung GY, Gasson JC, and Golde DW (1993). Identification and characterization of a high-affinity granulocyte-macrophage colony-stimulating factor receptor on primary rat oligodendrocytes. Blood 82, 3279–3282. [PubMed: 8241500]

Bennett ML, Bennett FC, Liddelow SA, Ajami B, Zamanian JL, Fernhoff NB, Mulinyawe SB, Bohlen CJ, Adil A, Tucker A, et al. (2016). New tools for studying microglia in the mouse and human CNS. Proc. Natl. Acad. Sci. USA 113, E1738–E1746. [PubMed: 26884166]

Berrebi D, Bruscoli S, Cohen N, Foussat A, Migliorati G, Bouchet-Delbos L, Maillot MC, Portier A, Couderc J, Galanaud P, et al. (2003). Synthesis of glucocorticoid-induced leucine zipper (GILZ) by macrophages: an anti-inflammatory and immunosuppressive mechanism shared by glucocorticoids and IL-10. Blood 101, 729–738. [PubMed: 12393603]

Biundo F, Ishiwari K, Del Prete D, and D'Adamio L (2016). Deletion of the γ-secretase subunits Aph1B/C impairs memory and worsens the deficits of knock-in mice modeling the Alzheimer-like familial Danish dementia. Oncotarget 7, 11923–11944. [PubMed: 26942869]

Bray NL, Pimentel H, Melsted P, and Pachter L (2016). Near-optimal probabilistic RNA-seq quantification. Nat. Biotechnol 34, 525–527. [PubMed: 27043002]

Butovsky O, Jedrychowski MP, Moore CS, Cialic R, Lanser AJ, Gabriely G, Koeglsperger T, Dake B, Wu PM, Doykan CE, et al. (2014). Identification of a unique TGF-β-dependent molecular and functional signature in microglia. Nat. Neurosci 17, 131–143. [PubMed: 24316888]

Chitu V, Gokhan S, Gulinello M, Branch CA, Patil M, Basu R, Stoddart C, Mehler MF, and Stanley ER (2015). Phenotypic characterization of a Csf1r haploinsufficient mouse model of adult-onset leukodystrophy with axonal spheroids and pigmented glia (ALSP). Neurobiol. Dis 74, 219–228. [PubMed: 25497733]

Chitu V, Gokhan Sx., Nandi S, Mehler MF, and Stanley ER (2016). Emerging Roles for CSF-1 Receptor and its Ligands in the Nervous System. Trends Neurosci. 39, 378–393. [PubMed: 27083478]

Croxford AL, Lanzinger M, Hartmann FJ, Schreiner B, Mair F, Pelczar P, Clausen BE, Jung S, Greter M, and Becher B (2015). The Cytokine GM-CSF Drives the Inflammatory Signature of CCR2+ Monocytes and Licenses Autoimmunity. Immunity 43, 502–514. [PubMed: 26341401]

Dai XM, Ryan GR, Hapel AJ, Dominguez MG, Russell RG, Kapp S, Sylvestre V, and Stanley ER (2002). Targeted disruption of the mouse colony-stimulating factor 1 receptor gene results in osteopetrosis, mononuclear phagocyte deficiency, increased primitive progenitor cell frequencies, and reproductive defects. Blood 99, 111–120. [PubMed: 11756160]

Doty RL, Brugger WE, Jurs PC, Orndorff MA, Snyder PJ, and Lowry LD (1978). Intranasal trigeminal stimulation from odorous volatiles: psychometric responses from anosmic and normal humans. Physiol. Behav 20, 175–185. [PubMed: 662939]

Dranoff G, Crawford AD, Sadelain M, Ream B, Rashid A, Bronson RT, Dickersin GR, Bachurski CJ, Mark EL, Whitsett JA, et al. (1994). Involvement of granulocyte-macrophage colony-stimulating factor in pulmonary homeostasis. Science 264, 713–716. [PubMed: 8171324]

Ennaceur A, and Delacour J (1988). A new one-trial test for neurobiological studies of memory in rats. 1: Behavioral data. Behav. Brain Res 31, 47–59. [PubMed: 3228475]

Fischer HG, Bielinsky AK, Nitzgen B, Däubener W, and Hadding U (1993). Functional dichotomy of mouse microglia developed in vitro: differential effects of macrophage and granulocyte/macrophage colony-stimulating factor on cytokine secretion and antitoxoplasmic activity. J. Neuroimmunol 45, 193–201. [PubMed: 8331161]

Flytzani S, Stridh P, Guerreiro-Cacais AO, Marta M, Hedreul MT, Jagodic M, and Olsson T (2013). Anti-MOG antibodies are under polygenic regulation with the most significant control coming from the C-type lectin-like gene locus. Genes Immun. 14, 409–419. [PubMed: 23784360]

Friedman BA, Srinivasan K, Ayalon G, Meilandt WJ, Lin H, Huntley MA, Cao Y, Lee SH, Haddick PCG, Ngu H, et al. (2018). Diverse Brain Myeloid Expression Profiles Reveal Distinct Microglial Activation States and Aspects of Alzheimer's Disease Not Evident in Mouse Models. Cell Rep. 22, 832–847. [PubMed: 29346778]

Georgoudaki AM, Khodabandeh S, Puiac S, Persson CM, Larsson MK, Lind M, Hammarfjord O, Nabatti TH, Wallin RP, Yrlid U, et al. (2015). CD244 is expressed on dendritic cells and regulates their functions. Immunol. Cell Biol 93, 581–590. [PubMed: 25643613]

Goldmann T, Wieghofer P, Müller PF, Wolf Y, Varol D, Yona S, Brendecke SM, Kierdorf K, Staszewski O, Datta M, et al. (2013). A new type of microglia gene targeting shows TAK1 to be pivotal in CNS autoimmune inflammation. Nat. Neurosci 16, 1618–1626. [PubMed: 24077561]

Gong Y, Sasidharan N, Laheji F, Frosch M, Musolino P, Tanzi R, Kim DY, Biffi A, El Khoury J, and Eichler F (2017). Microglial dysfunction as a key pathological change in adrenomyeloneuropathy. Ann. Neurol 82, 813–827. [PubMed: 29059709]

Greter M, Lelios I, and Croxford AL (2015). Microglia Versus Myeloid Cell Nomenclature during Brain Inflammation. Front. Immunol 6, 249. [PubMed: 26074918]

Gulinello M, Chen F, and Dobrenis K (2008). Early deficits in motor coordination and cognitive dysfunction in a mouse model of the neurodegenerative lysosomal storage disorder, Sandhoff disease. Behav. Brain Res 193, 315–319. [PubMed: 18611415]

Guyenet SJ, Furrer SA, Damian VM, Baughan TD, La Spada AR, and Garden GA (2010). A simple composite phenotype scoring system for evaluating mouse models of cerebellar ataxia. J. Vis. Exp (39), 1787. [PubMed: 20495529]

Habib GM, Shi ZZ, Cuevas AA, and Lieberman MW (2003). Identification of two additional members of the membrane-bound dipeptidase family. FASEB J. 17, 1313–1315. [PubMed: 12738806]

Hagemeyer N, Hanft KM, Akriditou MA, Unger N, Park ES, Stanley ER, Staszewski O, Dimou L, and Prinz M (2017). Microglia contribute to normal myelinogenesis and to oligodendrocyte progenitor maintenance during adulthood. Acta Neuropathol. 134, 441–458. [PubMed: 28685323]

Hajishengallis G, Reis ES, Mastellos DC, Ricklin D, and Lambris JD (2017). Novel mechanisms and functions of complement. Nat. Immunol 18, 1288–1298. [PubMed: 29144501]

Hansmann F, Herder V, Kalkuhl A, Haist V, Zhang N, Schaudien D, Deschl U, Baumgärtner W, and Ulrich R (2012). Matrix metalloproteinase-12 deficiency ameliorates the clinical course and demyelination in Theiler's murine encephalomyelitis. Acta Neuropathol 124, 127–142. [PubMed: 22271152]

Hegyi H (2017). Connecting myelin-related and synaptic dysfunction in schizophrenia with SNP-rich gene expression hubs. Sci. Rep 7, 45494. [PubMed: 28382934]

Hiebl V, Ladurner A, Latkolik S, and Dirsch VM (2018). Natural products as modulators of the nuclear receptors and metabolic sensors LXR, FXR and RXR. Biotechnol. Adv 36, 1657–1698. [PubMed: 29548878]

Hoppstädter J, Kessler SM, Bruscoli S, Huwer H, Riccardi C, and Kiemer AK (2015). Glucocorticoid-induced leucine zipper: a critical factor in macrophage endotoxin tolerance. J. Immunol 194, 6057–6067. [PubMed: 25964494]

Ip WKE, Hoshi N, Shouval DS, Snapper S, and Medzhitov R (2017). Anti-inflammatory effect of IL-10 mediated by metabolic reprogramming of macrophages. Science 356, 513–519. [PubMed: 28473584]

Jang J, Park S, Jin Hur H, Cho HJ, Hwang I, Pyo Kang Y, Im I, Lee H, Lee E, Yang W, et al. (2016). 25-hydroxycholesterol contributes to cerebral inflammation of X-linked adrenoleukodystrophy through activation of the NLRP3 inflammasome. Nat. Commun 7, 13129. [PubMed: 27779191]

Jiang T, Yu JT, Zhu XC, Tan MS, Gu LZ, Zhang YD, and Tan L (2014). Triggering receptor expressed on myeloid cells 2 knockdown exacerbates aging-related neuroinflammation and cognitive deficiency in senescence-accelerated mouse prone 8 mice. Neurobiol. Aging 35, 1243–1251. [PubMed: 24368090]

Keren-Shaul H, Spinrad A, Weiner A, Matcovitch-Natan O, Dvir-Szternfeld R, Ulland TK, David E, Baruch K, Lara-Astaiso D, Toth B, et al. (2017). A Unique Microglia Type Associated with Restricting Development of Alzheimer's Disease. Cell 169, 1276–1290.e17. [PubMed: 28602351]

Kimura T, Endo S, Inui M, Saitoh S, Miyake K, and Takai T (2015). Endoplasmic Protein Nogo-B (RTN4-B) Interacts with GRAMD4 and Regulates TLR9-Mediated Innate Immune Responses. J. Immunol 194, 5426–5436. [PubMed: 25917084]

Konno T, Tada M, Tada M, Koyama A, Nozaki H, Harigaya Y, Nishimiya J, Matsunaga A, Yoshikura N, Ishihara K, et al. (2014). Haploinsufficiency of CSF-1R and clinicopathologic characterization in patients with HDLS. Neurology 82, 139–148. [PubMed: 24336230]

Konno T, Kasanuki K, Ikeuchi T, Dickson DW, and Wszolek ZK (2018). *CSF1R*-related leukoencephalopathy: A major player in primary microgliopathies. Neurology 91, 1092–1104. [PubMed: 30429277]

Kostic M, Zivkovic N, Cvetanovic A, and Stojanovic I (2018). Granulocyte-macrophage colony-stimulating factor as a mediator of autoimmunity in multiple sclerosis. J. Neuroimmunol 323, 1–9. [PubMed: 30196820]

Krasemann S, Madore C, Cialic R, Baufeld C, Calcagno N, El Fatimy R, Beckers L, O'Loughlin E, Xu Y, Fanek Z, et al. (2017). The TREM2-APOE Pathway Drives the Transcriptional Phenotype of Dysfunctional Microglia in Neurodegenerative Diseases. Immunity 47, 566–581.e9. [PubMed: 28930663]

Kujuro Y, Suzuki N, and Kondo T (2010). Esophageal cancer-related gene 4 is a secreted inducer of cell senescence expressed by aged CNS precursor cells. Proc. Natl. Acad. Sci. USA 107, 8259–8264. [PubMed: 20404145]

Lang R, Patel D, Morris JJ, Rutschman RL, and Murray PJ (2002). Shaping gene expression in activated and resting primary macrophages by IL-10. J. Immunol 169, 2253–2263. [PubMed: 12193690]

Lapointe J, and Hekimi S (2008). Early mitochondrial dysfunction in long-lived Mclk1+/− mice. J. Biol. Chem 283, 26217–26227. [PubMed: 18635541]

Lee SC, Liu W, Brosnan CF, and Dickson DW (1994). GM-CSF promotes proliferation of human fetal and adult microglia in primary cultures. Glia 12, 309–318. [PubMed: 7890333]

Legroux L, Pittet CL, Beauseigle D, Deblois G, Prat A, and Arbour N (2015). An optimized method to process mouse CNS to simultaneously analyze neural cells and leukocytes by flow cytometry. J. Neurosci. Methods 247, 23–31. [PubMed: 25819540]

Li W, Liu X, Zhang B, Qi D, Zhang L, Jin Y, and Yang H (2010). Overexpression of candidate tumor suppressor ECRG4 inhibits glioma proliferation and invasion. J. Exp. Clin. Cancer Res 29, 89.

Lin WL, Wszolek ZK, and Dickson DW (2010). Hereditary diffuse leukoencephalopathy with spheroids: ultrastructural and immunoelectron microscopic studies. Int. J. Clin. Exp. Pathol 3, 665–674. [PubMed: 20830237]

Linnartz-Gerlach B, Bodea LG, Klaus C, Ginolhac A, Halder R, Sinkkonen L, Walter J, Colonna M, and Neumann H (2019). TREM2 triggers microglial density and age-related neuronal loss. Glia 67, 539–550. [PubMed: 30548312]

Liu Y, Wei Z, Ma X, Yang X, Chen Y, Sun L, Ma C, Miao QR, Hajjar DP, Han J, and Duan Y (2018). 25-Hydroxycholesterol activates the expression of cholesterol 25-hydroxylase in an LXR-dependent mechanism. J. Lipid Res 59, 439–451. [PubMed: 29298812]
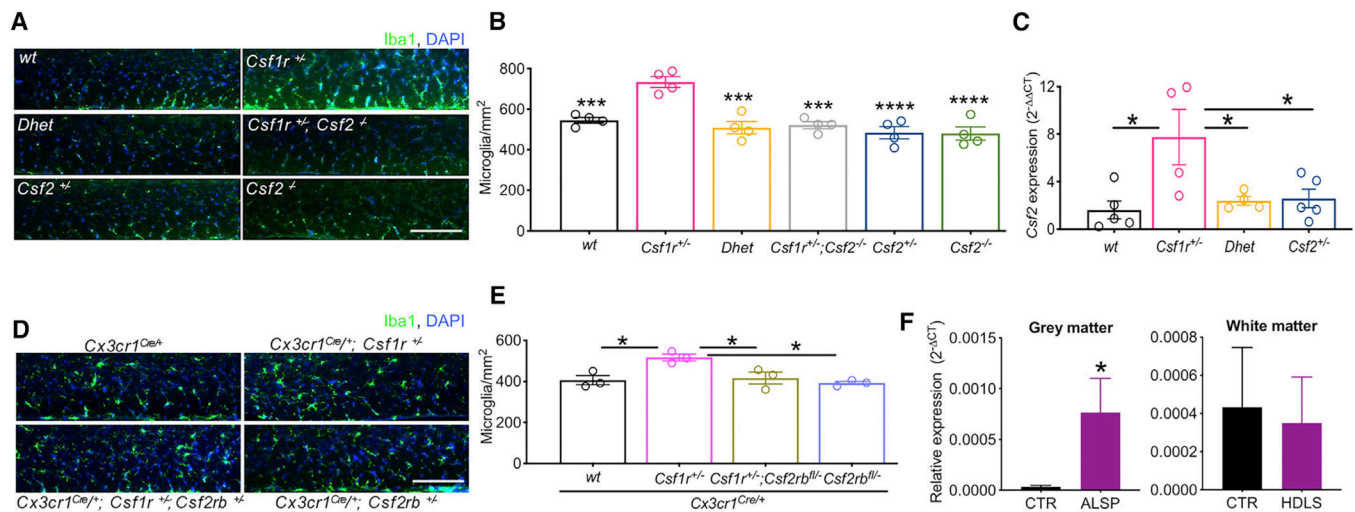
Lobo-Silva D, Carriche GM, Castro AG, Roque S, and Saraiva M (2016). Balancing the immune response in the brain: IL-10 and its regulation. J. Neuroinflammation 13, 297. [PubMed: 27881137]

Love MI, Huber W, and Anders S (2014). Moderated estimation of fold change and dispersion for RNA-seq data with DESeq2. Genome Biol. 15, 550. [PubMed: 25516281]

Ma J, Tanaka KF, Shimizu T, Bernard CC, Kakita A, Takahashi H, Pfeiffer SE, and Ikenaka K (2011). Microglial cystatin F expression is a sensitive indicator for ongoing demyelination with concurrent remyelination. J. Neurosci. Res 89, 639–649. [PubMed: 21344476]

Mathys H, Adaikkan C, Gao F, Young JZ, Manet E, Hemberg M, De Jager PL, Ransohoff RM, Regev A, and Tsai LH (2017). Temporal Tracking of Microglia Activation in Neurodegeneration at Single-Cell Resolution. Cell Rep. 21, 366–380. [PubMed: 29020624]

Mizutani M, Pino PA, Saederup N, Charo IF, Ransohoff RM, and Cardona AE (2012). The fractalkine receptor but not CCR2 is present on microglia from embryonic development throughout adulthood. J. Immunol 188, 29–36. [PubMed: 22079990]

Mori S, Maher P, and Conti B (2016). Neuroimmunology of the Interleukins 13 and 4. Brain Sci 6, 2.

Moriguchi T, Kaneumi S, Takeda S, Enomoto K, Mishra SK, Miki T, Koshimizu U, Kitamura H, and Kondo T (2016). Ecrg4 contributes to the anti-glioma immunosurveillance through type-I interferon signaling. OncoImmunology 5, e1242547. [PubMed: 28123880]

Mudge JM, and Harrow J (2015). Creating reference gene annotation for the mouse C57BL6/J genome assembly. Mamm. Genome 26, 366–378. [PubMed: 26187010]

Nicolas G, Charbonnier C, and Campion D (2016). From Common to Rare Variants: The Genetic Component of Alzheimer Disease. Hum. Hered 81, 129–141. [PubMed: 28002825]

Owens R, Grabert K, Davies CL, Alfieri A, Antel JP, Healy LM, and McColl BW (2017). Divergent Neuroinflammatory Regulation of Microglial TREM Expression and Involvement of NF-kB. Front. Cell. Neurosci 11, 56. [PubMed: 28303091]

Ozawa M, Sakatani M, Dobbs KB, Kannampuzha-Francis J, and Hansen PJ (2016). Regulation of gene expression in the bovine blastocyst by colony stimulating factor 2. BMC Res. Notes 9, 250. [PubMed: 27130208]

Peters A, and Folger Sethares C The Fine Structure of the Aging Brain. http://www.bu.edu/agingbrain.

Poliani PL, Wang Y, Fontana E, Robinette ML, Yamanishi Y, Gilfillan S, and Colonna M (2015). TREM2 sustains microglial expansion during aging and response to demyelination. J. Clin. Invest 125, 2161–2170. [PubMed: 25893602]

Porsolt RD, Bertin A, and Jalfre M (1977a). Behavioral despair in mice: a primary screening test for antidepressants. Arch. Int. Pharmacodyn. Ther 229, 327–336. [PubMed: 596982]

Porsolt RD, Le Pichon M, and Jalfre M (1977b). Depression: a new animal model sensitive to antidepressant treatments. Nature 266, 730–732. [PubMed: 559941]

Reed JA, Clegg DJ, Smith KB, Tolod-Richer EG, Matter EK, Picard LS, and Seeley RJ (2005). GM-CSF action in the CNS decreases food intake and body weight. J. Clin. Invest 115, 3035–3044. [PubMed: 16276414]

Roberts AW, Lee BL, Deguine J, John S, Shlomchik MJ, and Barton GM (2017). Tissue-Resident Macrophages Are Locally Programmed for Silent Clearance of Apoptotic Cells. Immunity 47, 913–927.e6. [PubMed: 29150239]

Rydbirk R, Folke J, Winge K, Aznar S, Pakkenberg B, and Brudek T (2016). Assessment of brain reference genes for RT-qPCR studies in neurodegenerative diseases. Sci. Rep 6, 37116. [PubMed: 27853238]

Saederup N, Cardona AE, Croft K, Mizutani M, Cotleur AC, Tsou CL, Ransohoff RM, and Charo IF (2010). Selective chemokine receptor usage by central nervous system myeloid cells in CCR2-red fluorescent protein knock-in mice. PLoS ONE 5, e13693. [PubMed: 21060874]

Safaiyan S, Kannaiyan N, Snaidero N, Brioschi S, Biber K, Yona S, Edinger AL, Jung S, Rossner MJ, and Simons M (2016). Age-related myelin degradation burdens the clearance function of microglia during aging. Nat. Neurosci 19, 995–998. [PubMed: 27294511]

Schäbitz WR, Krüger C, Pitzer C, Weber D, Laage R, Gassler N, Aronowski J, Mier W, Kirsch F, Dittgen T, et al. (2008). A neuroprotective function for the hematopoietic protein granulocyte-

macrophage colony stimulating factor (GM-CSF). J. Cereb. Blood Flow Metab 28, 29–43. [PubMed: 17457367]

Schindelin J, Arganda-Carreras I, Frise E, Kaynig V, Longair M, Pietzsch T, Preibisch S, Rueden C, Saalfeld S, Schmid B, et al. (2012). Fiji: an open-source platform for biological-image analysis. Nat. Methods 9, 676–682. [PubMed: 22743772]

Shin YJ, Kim HL, Choi JS, Choi JY, Cha JH, and Lee MY (2011). Osteopontin: correlation with phagocytosis by brain macrophages in a rat model of stroke. Glia 59, 413–423. [PubMed: 21264948]

Shrestha R, Millington O, Brewer J, Dev KK, and Bushell TJ (2014). Lymphocyte-mediated neuroprotection in in vitro models of excitotoxicity involves astrocytic activation and the inhibition of MAP kinase signalling pathways. Neuropharmacology 76, 184–193. [PubMed: 23831681]

Smith ME (1993). Phagocytosis of myelin by microglia in vitro. J. Neurosci. Res 35, 480–487. [PubMed: 7690856]

Spath S, Komuczki J, Hermann M, Pelczar P, Mair F, Schreiner B, and Becher B (2017). Dysregulation of the Cytokine GM-CSF Induces Spontaneous Phagocyte Invasion and Immunopathology in the Central Nervous System. Immunity 46, 245–260. [PubMed: 28228281]

Stephan AH, Barres BA, and Stevens B (2012). The complement system: an unexpected role in synaptic pruning during development and disease. Annu. Rev. Neurosci 35, 369–389. [PubMed: 22715882]

Stock AT, Hansen JA, Sleeman MA, McKenzie BS, and Wicks IP (2016). GM-CSF primes cardiac inflammation in a mouse model of Kawasaki disease. J. Exp. Med 213, 1983–1998. [PubMed: 27595596]

Sultan M, Piccini I, Balzereit D, Herwig R, Saran NG, Lehrach H, Reeves RH, and Yaspo ML (2007). Gene expression variation in Down's syndrome mice allows prioritization of candidate genes. Genome Biol. 8, R91. [PubMed: 17531092]

Tada M, Konno T, Tada M, Tezuka T, Miura T, Mezaki N, Okazaki K, Arakawa M, Itoh K, Yamamoto T, et al. (2016). Characteristic microglial features in patients with hereditary diffuse leukoencephalopathy with spheroids. Ann. Neurol 80, 554–565. [PubMed: 27490250]

Tarkowski E, Wallin A, Regland B, Blennow K, and Tarkowski A (2001). Local and systemic GM-CSF increase in Alzheimer's disease and vascular dementia. Acta Neurol. Scand 103, 166–174. [PubMed: 11240564]

Tian F, Wu CL, Yu BL, Liu L, and Hu JR (2017). Apolipoprotein O expression in mouse liver enhances hepatic lipid accumulation by impairing mitochondrial function. Biochem. Biophys. Res. Commun 491, 8–14. [PubMed: 28647361]

Torisu K, Zhang X, Nonaka M, Kaji T, Tsuchimoto D, Kajitani K, Sakumi K, Torisu T, Chida K, Sueishi K, et al. (2016). PKCh deficiency improves lipid metabolism and atherosclerosis in apolipoprotein E-deficient mice. Genes Cells 21, 1030–1048. [PubMed: 27545963]

Turkieh A, Caubè re C, Barutaut M, Desmoulin F, Harmancey R, Galinier M, Berry M, Dambrin C, Polidori C, Casteilla L, et al. (2014). Apolipoprotein O is mitochondrial and promotes lipotoxicity in heart. J. Clin. Invest 124, 2277–2286. [PubMed: 24743151]

Ulland TK, Song WM, Huang SC, Ulrich JD, Sergushichev A, Beatty WL, Loboda AA, Zhou Y, Cairns NJ, Kambal A, et al. (2017). TREM2 Maintains Microglial Metabolic Fitness in Alzheimer's Disease. Cell 170, 649–663.e13. [PubMed: 28802038]

Wahli W, and Michalik L (2012). PPARs at the crossroads of lipid signaling and inflammation. Trends Endocrinol. Metab 23, 351–363. [PubMed: 22704720]

Wang P, Mokhtari R, Pedrosa E, Kirschenbaum M, Bayrak C, Zheng D, and Lachman HM (2017). CRISPR/Cas9-mediated heterozygous knockout of the autism gene CHD8 and characterization of its transcriptional networks in cerebral organoids derived from iPS cells. Mol. Autism 8, 11. [PubMed: 28321286]

Wang Y, Liu N, and Lu B (2019). Mechanisms and roles of mitophagy in neurodegenerative diseases. CNS Neurosci. Ther 25, 859–875. [PubMed: 31050206]

Werner K, Bitsch A, Bunkowski S, Hemmerlein B, and Brück W (2002). The relative number of macrophages/microglia expressing macrophage colony-stimulating factor and its receptor decreases in multiple sclerosis lesions. Glia 40, 121–129. [PubMed: 12237849]
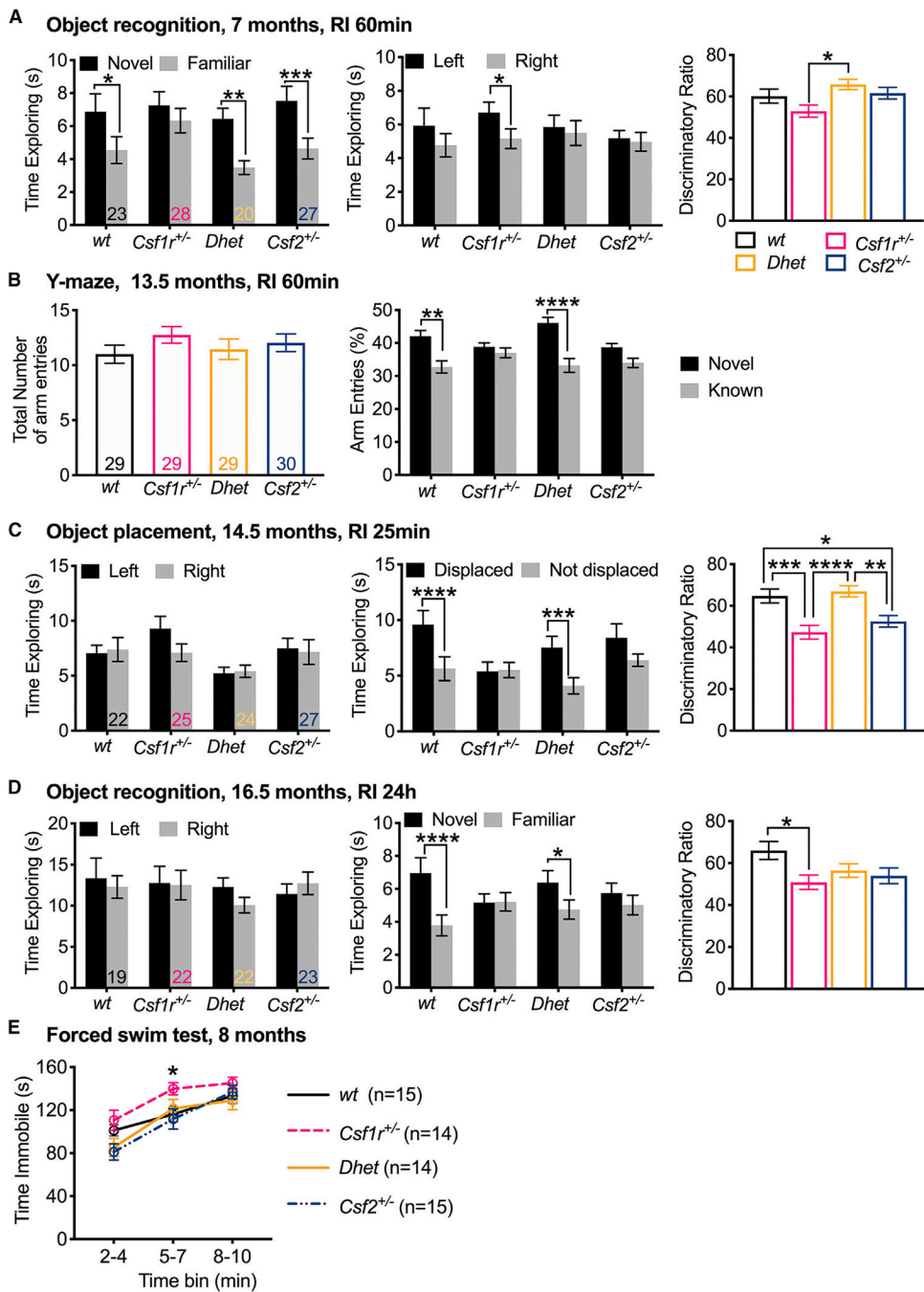
Witt RM, Galligan MM, Despinoy JR, and Segal R (2009). Olfactory behavioral testing in the adult mouse. J. Vis. Exp (23), 949. [PubMed: 19229182]

Wolter J, Schild L, Bock F, Hellwig A, Gadi I, Al-Dabet MM, Ranjan S, Rönicke R, Nawroth PP, Petersen KU, et al. (2016). Thrombomodulindependent protein C activation is required for mitochondrial function and myelination in the central nervous system. J. Thromb. Haemost 14, 2212–2226. [PubMed: 27590316]

Wu SP, Kao CY, Wang L, Creighton CJ, Yang J, Donti TR, Harmancey R, Vasquez HG, Graham BH, Bellen HJ, et al. (2015). Increased COUP-TFII expression in adult hearts induces mitochondrial dysfunction resulting in heart failure. Nat. Commun 6, 8245. [PubMed: 26356605]

Xiang Y, Tang JJ, Tao W, Cao X, Song BL, and Zhong J (2015). Identification of Cholesterol 25-Hydroxylase as a Novel Host Restriction Factor and a Part of the Primary Innate Immune Responses against Hepatitis C Virus Infection. J. Virol 89, 6805–6816. [PubMed: 25903345]

Yona S, Kim KW, Wolf Y, Mildner A, Varol D, Breker M, Strauss-Ayali D, Viukov S, Guilliams M, Misharin A, et al. (2013). Fate mapping reveals origins and dynamics of monocytes and tissue macrophages under homeostasis. Immunity 38, 79–91. [PubMed: 23273845]

Young K, and Morrison H (2018). Quantifying Microglia Morphology from Photomicrographs of Immunohistochemistry Prepared Tissue Using ImageJ. J. Vis. Exp (136)

Zeisel A, Yitzhaky A, Bossel Ben-Moshe N, and Domany E (2013). An accessible database for mouse and human whole transcriptome qPCR primers. Bioinformatics 29, 1355–1356. [PubMed: 23539303]

Zhang H, Meng F, Chu CL, Takai T, and Lowell CA (2005). The Src family kinases Hck and Fgr negatively regulate neutrophil and dendritic cell chemokine signaling via PIR-B. Immunity 22, 235–246. [PubMed: 15723811]

Highlights

- ALSP is a *CSF1R*-deficiency dementia associated with increased *CSF2* expression

- In *Csf1r*$^{+/-}$ ALSP mice, CSF-2 promotes microgliosis by direct signaling in microglia

- Targeting *Csf2* improves cognition and myelination and normalizes microglial function

- CSF-2 is a therapeutic target in ALSP

Figure 1. Involvement of CSF-2 in the Pathology of ALSP

(A) Microglial densities in the *corpus callosum* of 4- to 5-month-old mice.

(B) Quantification of microglial densities. Two-way ANOVA followed by Dunnett's post hoc test.

(C) Restoration of normal *Csf2* expression in 3- to 4-month-old *Csf1r*$^{+/-}$ mice by monallelic targeting of *Csf2*. One-way ANOVA followed by Tukey's multiple comparisons test.

(D and E) Evidence of direct regulation of the increase of Iba1$^+$ cell density by Csf2. Microglial densities (D) and quantification (E). Data ± SEM, 3-month-old mice, one-way ANOVA followed by Tukey's multiple comparisons test.

(F) Expression of *CSF2* in the periventricular white matter and adjacent gray matter of ALSP patients and healthy controls, determined by real-time qPCR and normalized to *RPL13*. n = 5 control or ALSP specimens; *p < 0.05, one- tailed Student's t test.

Scale bars, 100 μm, applies to all panels in the corresponding composite image. Data are presented as means ± SEM, and only the significantly different changes are marked by asterisks. See also Figure S1 and Tables S1 and S9.

A Object recognition, 7 months, RI 60min

B Y-maze, 13.5 months, RI 60min

C Object placement, 14.5 months, RI 25min

D Object recognition, 16.5 months, RI 24h

E Forced swim test, 8 months

Figure 2. Deletion of a Single *Csf2* Allele Prevents the Cognitive Deficit and Depression in ALSP (*Csf1r*$^{+/-}$) Mice

(A–D) Cognitive assessment. The test performed, age of the mice, and retention interval (RI) are indicated in each panel. The number of mice per genotype in each experiment is shown in the bars in the left panel.

(A) Left (training): preference for the left side by *Csf1r*$^{+/-}$ mice exploring two familiar identical objects. Right (testing): *Csf1r*$^{+/-}$ mice spent less time exploring the novel object (left side).

(B) Left: similar exploration of the arms of the Y-maze in all experimental groups. Right: lower discrimination for the novel arm by *Csf1r*$^{+/-}$ mice is corrected in *Csf1r*$^{+/-}$; *Csf2*$^{+/-}$ (*Dhet*) mice.

(C) Left: all experimental groups exhibited similar times of exploration of either object. Right: lower preference for the displaced object by *Csf1r*$^{+/-}$ mice is corrected in *Dhet* mice.

(D) Left (training): all experimental groups exhibited similar times of exploration of two familiar identical objects. Right (testing): reduced long-term memory for the novel object by *Csf1r*$^{+/-}$ mice was corrected in *Dhet* mice.

(E) Increased depression-like behavior in male *Csf1r*$^{+/-}$ mice is corrected in *Dhet* mice.

Data were analyzed using two-way ANOVA followed by Bonferroni's (A–C); Holm-Sidak's (D); or Benjamini, Krieger, and Yekutieli's (E) post hoc tests. The left panel in (B) was analyzed by one-way ANOVA (not significant). Data are presented as means ± SEM.

See also Figure S2 and Table S9.
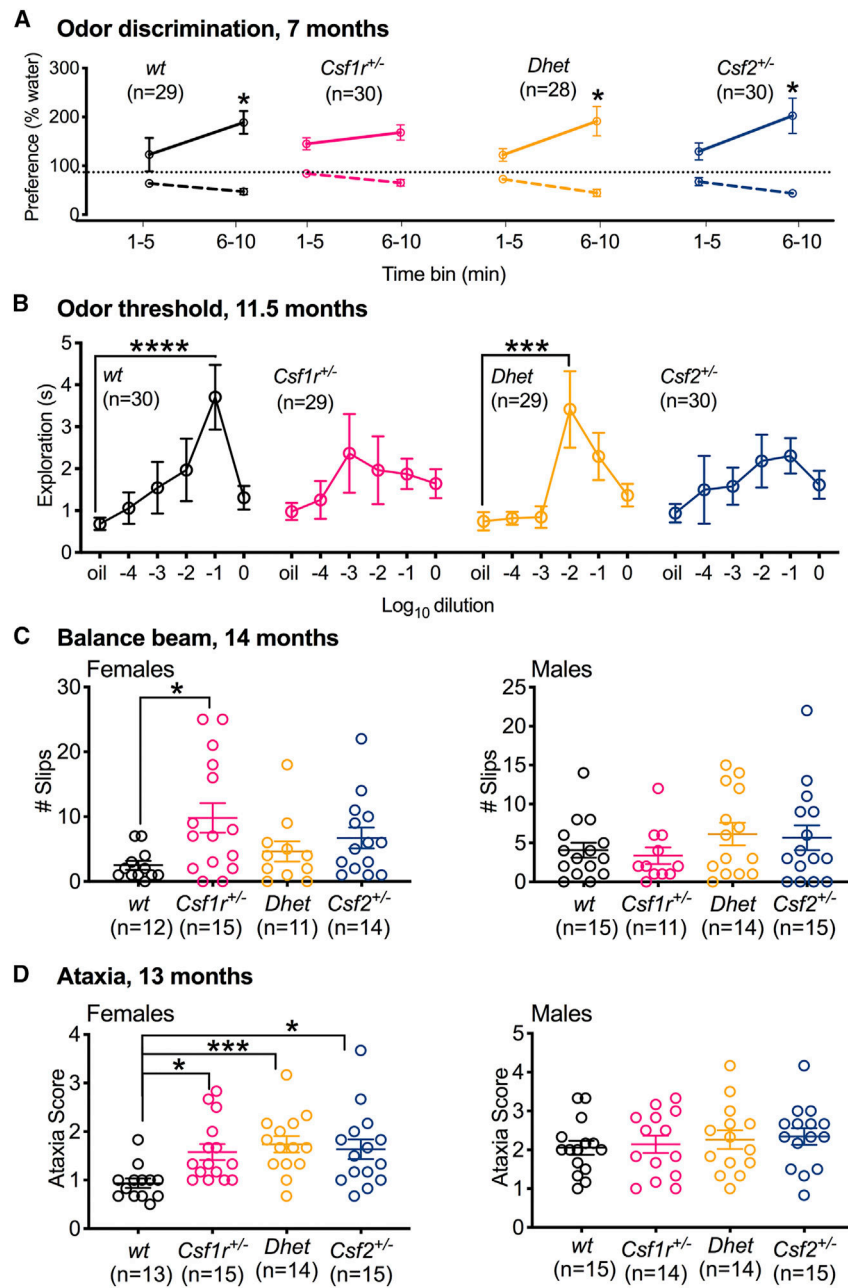
Figure 3. Attenuation of the Olfactory and Motor Coordination Deficits of *Csf1r*^{+/−} Mice by *Csf2* Heterozygosity

(A) Odor discrimination at 7 months of age. *Csf1r*^{+/−} mice showed no significant increase in exploring the pure odorant vanilla.

(B) Odor threshold to the pure odorant 2-phenylethanol by 11.5-month-old mice. Absence of a significant threshold in *Csf1r*^{+/−} mice is corrected in *Dhet* mice.

(C) Locomotor coordination in mice, assessed as number of slips in the balance beam test.

(D) Ataxia score in mice, assessed as sum of the ledge, hindlimb, and gait scores.

Data were analyzed using two-way ANOVA followed by Bonferroni's (A) and Dunnett's (B) post hoc tests or by Kruskal-Wallis test followed by Dunn's post hoc tests (C and D). Data are presented as means ± SEM.

See also Figure S2 and Table S9.
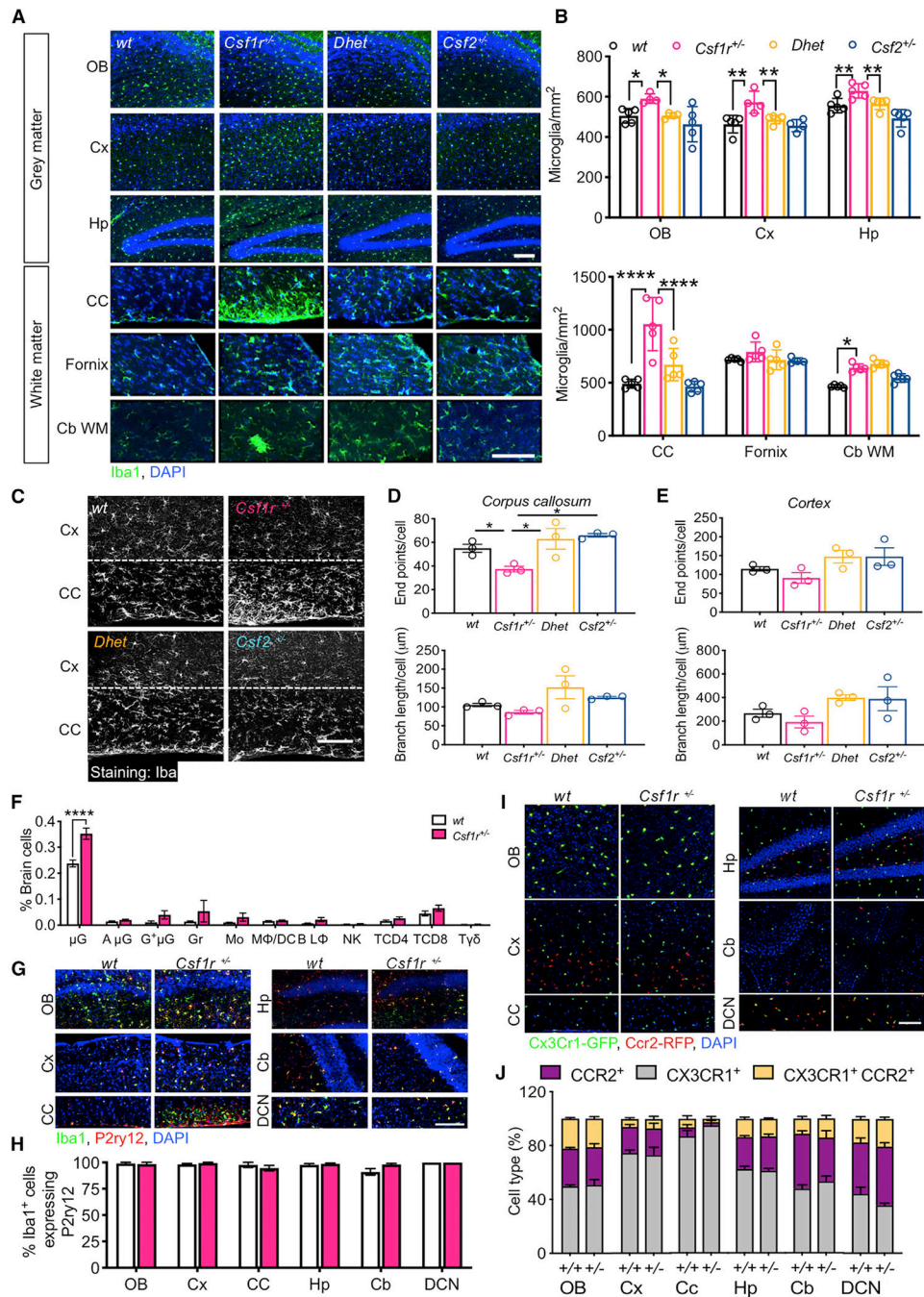
Figure 4. *Csf2* **Heterozygosity Prevents Cerebral Microgliosis in Aged ALSP Mice**

(A) Iba1$^+$ cell densities (green) in different areas of brains of 18-month-old mice. Cb, cerebellum; CC, *corpus callosum*; Cb WM, cerebellar white matter; Cx, primary motor cortex; DCN, deep cerebellar nuclei; Hp, hippocampus; OB, olfactory bulb.

(B) Quantification of Iba1$^+$ cell densities.

(C) Morphology of Iba1$^+$ cells. The dotted line indicates the border between the CC and the adjacent gray matter.

(D and E) Quantification of microglia ramification in the white (D) and gray (E) matter regions shown in (C).

(F) Quantification of microglia and infiltrating leukocytes by flow cytometry. μG, microglia; AμG, activated microglia; BLΦ, B lymphocytes; $G^+μG$, $Ly6G^+$ $P2ry12^{high}$ microglia; Gr, $Ly6G^+P2ry12^-$ granulocytes; MΦ/DC, $Ly6C^-$ macrophages/dendritic cells; Mo, $Ly6C^+$ infiltrated monocytes; NK, natural killer cells; TCD4 and TCD8, CD4 and $CD8^+$ T lymphocytes; Tγδ, γδ T cells. Data were obtained from 16-month-old WT (n = 4) and $Csf1r^{+/-}$ (n = 5) mice.

(G) Colocalization of P2ry12 (red) with $Iba1^+$ cells (green).

(H) Quantification of P2ry12 expression in $Iba1^+$ cells in WT and $Csf1r^{+/-}$ mice; 5 mice/ genotype.

(I) Expression of *Cx3Cr1* (GFP, green) and *Ccr2* (RFP, red) reporters in 11-month-old $Cx3Cr1^{GFP/+};Ccr2^{RFP/+};Csf1r^{+/+}$ (+/+) and $Cx3Cr1^{GFP/+};Ccr2^{RFP/+};Csf1r^{+/-}$ (+/−) mice.

(J) Quantification of mononuclear phagocytes in $Cx3Cr1^{GFP/+};Ccr2^{RFP/+}$ reporter mice (5 mice/genotype). Significance was analyzed using two-way ANOVA (B, F, H, and J) or one-way ANOVA (D and E), followed by Benjamini Krieger and Yekutieli post hoc analyses. Data are presented as means ± SEM. Scale bars, 100 μm, apply to all panels in the corresponding composite image. Minor irregularities in (A) images $Csf2^{+/-}$ Cx and $Csf1r^{+/-}$ CC, (G) images $Csf1r^{+/-}$ Hp and WT Cb, and (I) *WT* and $Csf1r^{+/-}$ Cb images arise from automated image stitching in Photoshop.

See also Figures S3 and S4 and Table S9.
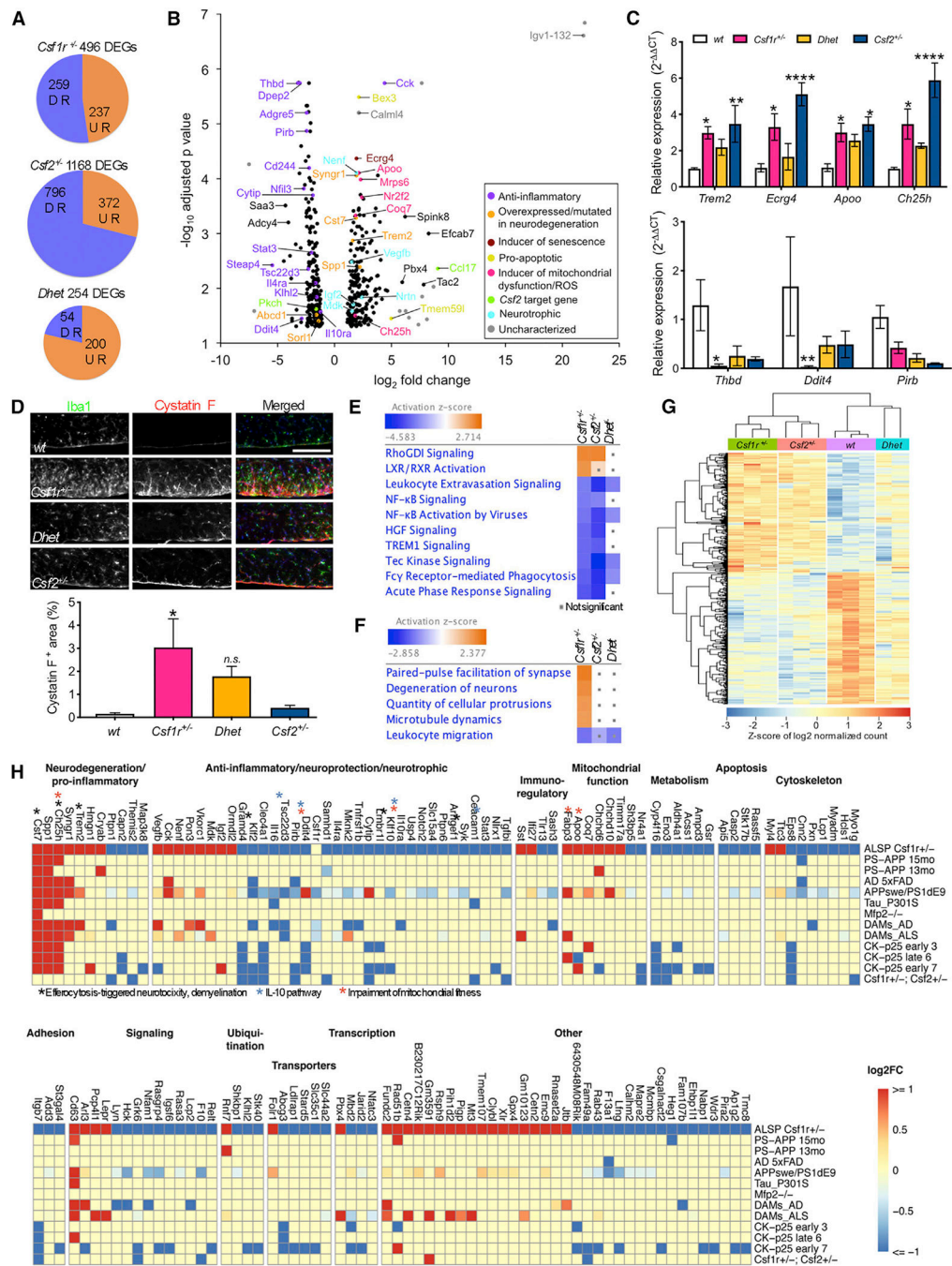
Figure 5. *Csf2* Heterozygosity Restores the *Csf1r*^{+/−} Microglial Transcriptomics Profile

(A) Differences in gene expression profile in *Csf1r*^{+/−}, *Csf2*^{+/−}, and *Dhet* microglia compared with WT controls.

(B) Volcano plot highlighting DEGs of interest in *Csf1r*^{+/−} microglia.

(C) Validation of changes in expression of selected upregulated (top panel) and downregulated (lower panel) genes in microglia isolated from 4 WT, 5 *Csf1r*^{+/−}, 5 *Dhet*, and 4 *Csf2*^{+/−} mice. Two-way ANOVA followed by Dunnett's post hoc test.

(D) Expression of Cystatin F in the CC of WT, single heterozygous, and Dhet mice. Scale bar, 100 μm, applies to all panels. N = 5 mice/genotype, one-way ANOVA followed by Tukey's post hoc test; n.s., not significant (p = 0.33).

(E and F) Ingenuity Pathway Analysis (IPA)-generated list of pathways (E) and biological processes (F) affected by *Csf1r* heterozygosity and their predicted activation status in *Csf2*$^{+/-}$ and *Dhet* microglia. Dots indicate no significant difference.

(G) Heatmap showing the expression of *Csf1r*$^{+/-}$ DEGs across individual samples.

(H) Illustration of the overlap of *Csf1r*$^{+/-}$ DEGs with genes differentially expressed in other mouse models of neurodegenerative disease. Note decreased *Csf1r* expression in a model of Alzheimer's disease (AD) (APPswe/PS1dEp) and in disease-associated microglia (DAMs-AD, DAMs-ALS). The *Csf1r* targeting strategy (Dai et al., 2002) does not affect transcription, precluding confident detection of decreased *Csf1r* expression in *Csf1r*$^{+/-}$ microglia using RNA sequencing (RNA-seq) (log$_2$FC = −1.15, p = 0.01, adjusted p = 0.1). Data are presented as means ± SEM.

See also Figure S5 and Tables S2, S3, and S4–S10.
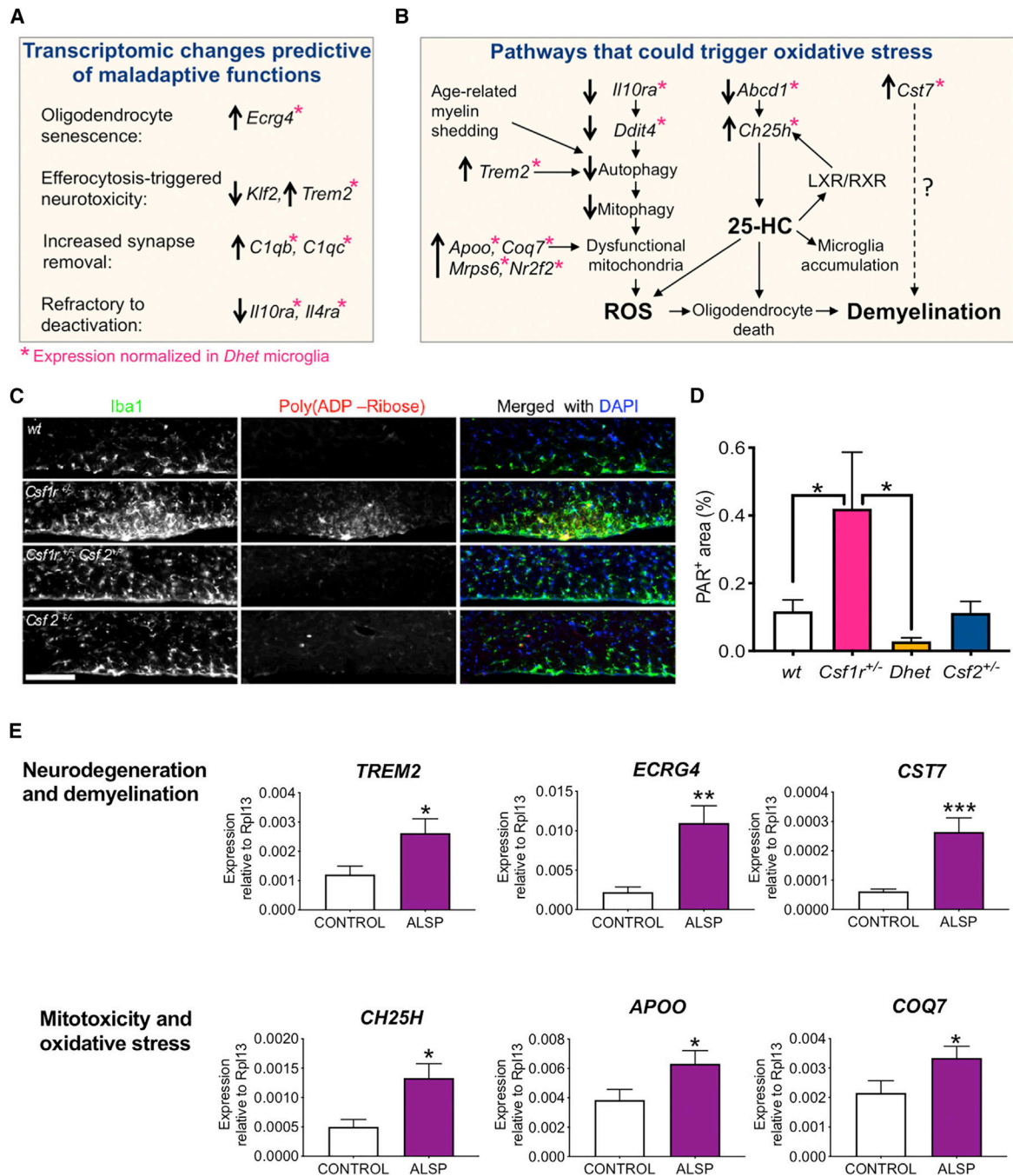
Figure 6. Pathways Dysregulated in *Csf1r*^{+/−} Mice and ALSP Patients

(A and B) Predicted maladaptive functions (A) and hypothetical pathways (B) dysregulated in *Csf1r*^{+/−} mouse microglia.

(C) Evidence of oxidative stress: colocalization of the poly (ADP-ribose) signal with callosal microglial patches in periventricular white matter. Scale bar, 100 μm, applies to all panels.

(D) Quantification of the callosal area positive for poly (ADP-Ribose) in 2–3 sections/ mouse, 5–9 mice/genotype. One-way ANOVA followed by Kruskal-Wallis test.

(E) Transcriptomics changes potentially critical for pathology also occur in the periventricular white matter of ALSP patients (n = 5); *p < 0.05, one- tailed Student's t test. Data are presented as means ± SEM.

See also Tables S9 and S10.
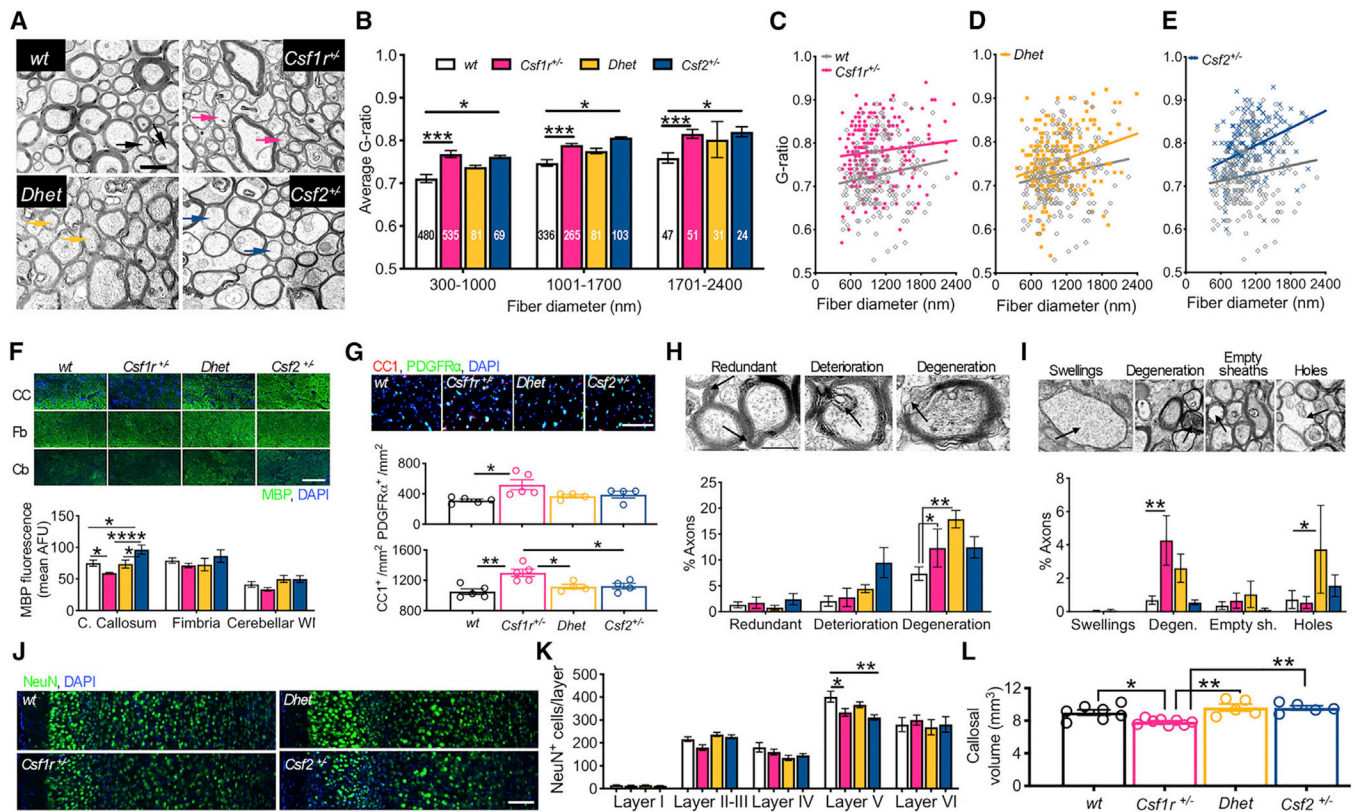
Figure 7. *Csf2* **Heterozygosity in ALSP Mice Prevents Callosal Atrophy and Improves Myelination**

(A) Myelin and axonal ultrastructure in callosal cross-sections from 9- to 11-month-old mice. Arrows point to examples of changes in myelin thickness in axons of small and medium diameters.

(B–E) Changes in G-ratio in *Csf1r*^{+/−} (B and C) and *Csf2*^{+/−} (B and E) mice are attenuated by double heterozygosity (B and D). (B) shows average values per mouse (2–6 mice/genotype); values in the bars indicate the total numbers of fibers examined in each fiber diameter range. (C)–(E) show individual G-ratio values.

(F) Quantification of MBP staining in white matter tracts, including CC, fimbria (Fb), and Cb. n = 3–7 mice/genotype.

(G) Changes in myelination are not accompanied by a decrease in early oligodendrocyte precursors (PDGFRα[+]) or oligodendrocytes (CC1^{+}).

(H) Quantification of age-induced myelin pathology in WT and mutant mice (2–7 mice/genotype, >900 neurons/genotype). The top panels show representative examples of structural abnormalities.

(I) Quantification of age-induced axonal pathology in WT and mutant mice (data from 3–6 mice/genotype, >900 neurons/genotype). The top panels show representative examples of structural abnormalities.

(J) Neuronal loss in cortical layer V at 18 months of age. Scale bar, 100 μm.

(K) Average NeuN-positive cells per layer. n = 4 mice/genotype.

(L) *Csf2* heterozygosity prevents callosal atrophy in 19-month-old *Csf1r*^{+/−} mice.

Significance was analyzed using two-way ANOVA followed by Holm-Sidak's (B, F, and K) or Benjamini, Krieger, and Yekutieli's (H and I) post hoc tests and one-way ANOVA followed by Tukey's post hoc test (H and L). Scale bars, 1 μm (A), 50 μm (F), 100 μm (G and J), and 500 nm (H and I); apply to all images in the corresponding panels. Data are presented as means ± SEM.

See also Table S9.

KEY RESOURCES TABLE

REAGENT or RESOURCE	SOURCE	IDENTIFIER
Antibodies		
Anti-mouse CD16/CD32 (Mouse BD Fc Block)	BD	Cat#533142; RRID: AB_394657
Anti-mouse CD45 APC-Cy7 (clone 30-F11)	BD	Cat#557659; RRID: AB_396774
Anti-mouse Ly6G BV605 (clone 1A8)	BioLegend	Cat# 127639, RRID:AB_2565880
Anti-mouse /human CD11b BV510 (clone M1/70)	BioLegend	Cat#101263; RRID: AB_2629529
Anti-mouse P2RY12 PE (clone S16007)	BioLegend	Cat#848004, RRID:AB_2721645
Anti-mouse CD11c APC (clone N418)	BioLegend	Cat# 117309, RRID:AB_313778
Anti-mouse Ly-6C BV711 (clone HK1.4)	BioLegend	Cat# 128037, RRID:AB_2562630
Anti-mouse CD19 Alexa 700 (clone 6D5)	BioLegend	Cat# 115527, RRID:AB_493734
Anti-mouse NK-1.1 BV785 (clone PK136)	BioLegend	Cat# 108749, RRID:AB_2564304
Anti-mouse CD3 PE/Cy7 (clone 17A2)	BioLegend	Cat# 100219, RRID:AB_1732068
Anti-mouse TCRγδ BV421 (clone GL3)	BioLegend	Cat# 118119, RRID:AB_10896753
Anti-mouse CD4 PerCP-eFluor 710 (clone GK1.5)	Invitrogen	Cat# 44-0041-82; RRID:AB_11150050
Anti-mouse CD8a FITC (clone 53-6.7)	BioLegend	Cat# 100705, RRID:AB_312744
Anti-Iba1, Rabbit	Wako	Cat# 019-19741, RRID:AB_839504
Anti-Iba1, Goat	AbCam	Cat# ab107159, RRID:AB_10972670
Anti-P2RY12, Rat	Dr. O. Butovsky	Gift
Anti-MBP (Smi99), Mouse	BioLegend	Cat# 808401, RRID:AB_2564741
Anti-APC (CC1), Mouse	Millipore	Cat# OP80, RRID:AB_2057371
Anti-PDGFRα, Goat	R and D Systems	Cat# AF1062, RRID:AB_2236897
Anti-CST7, Rabbit	Bioss	Cat# bs-6039R, RRID:AB_11073757
Anti-Poly ADP-ribose (Clone H10), Mouse	Millipore	Cat# MABC547, RRID:N/A
Anti-NeuN, Mouse	BioLegend	Cat# MAB377X, RRID:AB_2149209
Biological Samples		
Human brain tissue samples	Mayo Clinic, FL	N/A
Experimental Models: Organisms/Strains		
C57/BL6 CSF-1R knockout mouse	Dai et al., 2002	N/A
C57/BL6 $Csf2^{+/-}$ mice	Dranoff et al., 1994	N/A
C57/BL6 $Csf2rb^{fl/fl}$ mice	Croxford et al., 2015	N/A
C57/BL6 $Cx3Cr1^{Cre/+}$ mice	Yona et al., 2013	N/A
C57/BL6 $Cx3Cr1^{GFP}; Ccr2^{RFP}$ reporter mouse	Saederup et al., 2010	N/A
Chemicals, Peptides, and Recombinant Proteins		
Fluoromyelin	Invitrogen	Cat# F34652
DAPI	Biolegend	Cat# 422801
Triton X-100	EMS	Cat# 22140
Tween 20	Sigma	Cat# P9416
Percoll	VWR	Cat# 17-0891-01

REAGENT or RESOURCE	SOURCE	IDENTIFIER
Myelin Removal Beads II	Milteny Biotec	Cat# 130-096-733
RNAsin	Promega	Cat# N2615
DNaseI, RNase-free	Thermo Scientific	Cat#EN0525
TRIzol	Thermo Fisher	Cat# 15596018
FCS	Atlanta Biologicals	Cat# S12450H
Donkey serum	Millipore	Cat# 566-460
Collagenase D	Roche Diagnostic	Cat# 11088866001
DNase I	Roche Diagnostic	Cat# 11284932001
Critical Commercial Assays		
Live/Dead Fixable Far Red Dead Cell Stain Kit	Invitrogen	Cat# L34973
RNEasy Plus Micro RNA Extraction Kit	QIAGEN	Cat# 74034
ProLong Gold Antifade with DAPI	Invitrogen	Cat# P36935
Mouse GM-CSF Quantikine ELISA	R&D Systems	Cat# MGM00
Oligonucleotides		
Human CSF2 PrimePCR Assay	BIO-RAD	Cat# 10025636 qHsaCED0002766
$Csf2^{+/-}$ mice genotyping forward wt: TCGTCTCTAACGAGTTCTCCTTCA	Dranoff et al., 1994	N/A
$Csf2^{+/-}$ mice genotyping reverse wt: TGCTCGAATATCTTCAGG	Dranoff et al., 1994	N/A
$Csf2^{+/-}$ mice genotyping reverse $Csf2$ KO: GGCCACTTGTGTAGCGCCAAGT	Dranoff et al., 1994	N/A
Primers for qPCR	See Table S10	N/A
Software and Algorithms		
ImageJ	Schindelin et al., 2012	http://fiji.sc/
Microglia morphometry algorithm	Young and Morrison, 2018	http://www.jove.com/video/57648/quantifying-microglia-morphology-from-photomicrographs
Other		
Collection of electron micrographs illustrating the effects of aging in the brain	(Peters and Folger Sethares)	http://www.bu.edu/agingbrain
Deposited Data		
Raw FACS data for Figure 4H	Mendeley Data	https://doi.org/10.17632/7m928vkpht.1
RNA Seq data	GEO	Accesion number GSE143823